The University of Maine

DigitalCommons@UMaine

Robust algorithm for estimating total suspended solids (TSS) in inland and nearshore coastal waters

Sundarabalan V. Balasubramanian
NASA Goddard Space Flight Center

Nima Pahlevan
NASA Goddard Space Flight Center

Brandon Smith
NASA Goddard Space Flight Center

Caren Binding
Environment Canada

John Schalles
Creighton University

See next page for additional authors

Follow this and additional works at: https://digitalcommons.library.umaine.edu/sms_facpub

🔵 Part of the Oceanography and Atmospheric Sciences and Meteorology Commons

Authors

Sundarabalan V. Balasubramanian, Nima Pahlevan, Brandon Smith, Caren Binding, John Schalles, Hubert Loisel, Daniela Gurlin, Steven Greb, Krista Alikas, Mirjam Randla, Matsushita Bunkei, Wesley Moses, Hà Nguyễn, Moritz K. Lehmann, David O'Donnell, Michael Ondrusek, Tai Hyun Han, Cédric G. Fichot, Tim Moore, and Emmanuel Boss
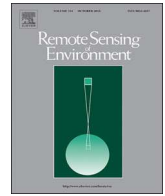
Robust algorithm for estimating total suspended solids (TSS) in inland and nearshore coastal waters

Sundarabalan V. Balasubramanian[a,c,d], Nima Pahlevan[a,b,*], Brandon Smith[a,b], Caren Binding[e], John Schalles[f], Hubert Loisel[g], Daniela Gurlin[h], Steven Greb[i], Krista Alikas[j], Mirjam Randla[j], Matsushita Bunkei[k], Wesley Moses[l], Hà Nguyễn[m], Moritz K. Lehmann[n], David O'Donnell[o], Michael Ondrusek[p], Tai-Hyun Han[q], Cédric G. Fichot[r], Tim Moore[s], Emmanuel Boss[t]

[a] NASA Goddard Space Flight Center, Greenbelt, MD, USA
[b] Science Systems and Applications, Inc. (SSAI), Lanham, MD, USA
[c] University of Maryland, Department of Geographical Sciences, College Park, MD, USA
[d] Geo-Sensing and Imaging Consultancy, Trivandrum, Kerala, India
[e] Environment and Climate Change Canada, Burlington, ON, Canada
[f] Creighton University, Department of Biology, Omaha, Nebraska, USA
[g] Univ. Littoral Côte d'Opale, Univ. Lille, CNRS, UMR 8187, LOG, Laboratoire d'Océanologie et de Géosciences, Lille, France
[h] Wisconsin Department of Natural Resources, Madison, WI, USA
[i] University of Wisconsin-Madison, Space Science and Engineering, Madison, WI, USA
[j] Tartu observatory of University of Tartu, Tartu, Estonia
[k] University of Tsukuba, Ibaraki, Japan
[l] Naval Research Laboratory, Washington, DC, USA
[m] VNU University of Science, Vietnam National University, Hanoi, Viet Nam
[n] Xerra Earth Observation Institute and the University of Waikato, Hamilton, New Zealand
[o] Upstate Freshwater Institute, Syracuse, NY, USA
[p] NOAA Center for Satellite Applications and Research, College Park, MD, USA
[q] Korea Ocean Satellite Center KIOST, Busan, South Korea
[r] Department of Earth and Environment, Boston University, Boston, MA, USA
[s] Ocean Process Analysis Laboratory, University of New Hampshire, Durham, NH, USA
[t] University of Maine, School of Marine Sciences, Orono, ME, USA

ARTICLE INFO

ABSTRACT

One of the challenging tasks in modern aquatic remote sensing is the retrieval of near-surface concentrations of Total Suspended Solids (TSS). This study aims to present a Statistical, inherent Optical property (IOP) -based, and muLti-conditional Inversion proceDure (SOLID) for enhanced retrievals of satellite-derived TSS under a wide range of in-water bio-optical conditions in rivers, lakes, estuaries, and coastal waters. In this study, using a large *in situ* database ($N > 3500$), the SOLID model is devised using a three-step procedure: (*a*) water-type classification of the input remote sensing reflectance (R_{rs}), (*b*) retrieval of particulate backscattering (b_{bp}) in the red or near-infrared (NIR) regions using semi-analytical, machine-learning, and empirical models, and (*c*) estimation of TSS from b_{bp} via water-type-specific empirical models. Using an independent subset of our *in situ* data ($N = 2729$) with TSS ranging from 0.1 to 2626.8 [g/m^3], the SOLID model is thoroughly examined and compared against several state-of-the-art algorithms (Miller and McKee, 2004; Nechad et al., 2010; Novoa et al., 2017; Ondrusek et al., 2012; Petus et al., 2010). We show that SOLID outperforms all the other models to varying degrees, i.e.,from 10 to > 100%, depending on the statistical attributes (e.g., global versus water-type-specific metrics). For demonstration purposes, the model is implemented for images acquired by the MultiSpectral Imager aboard Sentinel-2A/B over the Chesapeake Bay, San-Francisco-Bay-Delta Estuary, Lake Okeechobee, and Lake Taihu. To enable generating consistent, multimission TSS products, its performance is further extended to, and evaluated for, other missions, such as the Ocean and Land Color Instrument (OLCI), Moderate Resolution Imaging Spectroradiometer (MODIS), Visible Infrared Imaging Radiometer Suite (VIIRS), and Operational Land Imager (OLI). Sensitivity analyses on uncertainties induced by the atmospheric correction indicate that 10% uncertainty in R_{rs} leads to < 20% uncertainty in TSS retrievals from SOLID. While this study suggests that SOLID

has a potential for producing TSS products in global coastal and inland waters, our statistical analysis certainly verifies that there is still a need for improving retrievals across a wide spectrum of particle loads.

1. Introduction

Suspended sediments in coastal and inland waters are introduced by various sources, including river runoffs, dredging activities, resuspension events, and tidal currents. The sediment composition is, in general, a mixture of organic and inorganic particles in the water column (Miller and McKee, 2004). High sediment loads can lead to poor water quality and potentially increase temperature in the upper layer of the water column (Turner and Millward, 2002). Suspended solids can carry heavy metals, pollutants, and nutrients, and therefore, contribute to adverse environmental conditions in the water column. Excessive near-surface accumulation of this optically significant water constituent affects light propagation into deeper layers and the benthos, diminishing the productivity and altering the ecosystem function. Conversely, sediment loads are critical for maintaining sediment accretion rates and protecting the integrity of sediment-maintained geomorphic features such as river deltas and marsh and mangrove wetland platforms. These coastal features are damaged when sediment dynamics are compromised by upstream trapping of suspended sediments by reservoirs, river channelization and disturbance of delta distributary flows, and sea level rise. These geomorphic features support and protect blue-carbon storages of coastal wetland sediments and are important defenses against storm surge and high spring tide flooding events (Barbier et al., 2011; Weston, 2014). Monitoring sediment fluxes is, thus, essential for the sustainable management of coastal and inland water ecosystems.

The sediment concentration is commonly quantified via laboratory analyses of grab samples and expressed as the concentration of total suspended solids (TSS; $[g/m^3]$), which is also referred to as suspended particulate matter (SPM) and total suspended matter (TSM) in the literature. TSS includes living and detrital (non-living) particulate organic matter, such as phytoplankton, and inorganic matter like clay and other suspended minerals. Due to the dynamic nature of its spatial and temporal distribution, TSS quantified through field sampling is often considered inadequate (Doxaran et al., 2014); hence, aquatic (optical) remote sensing is used as an efficient proxy for its monitoring at local, regional, and global scales (Ahn et al., 2006; Bowers and Binding, 2006; Doxaran et al., 2009a; Feng et al., 2014; Forget and Ouillon, 1998; Loisel et al., 2014; Woźniak and Stramski, 2004). One of the main products of aquatic color remote sensing is the spectral remote sensing reflectance $R_{rs}(\lambda)$, which carries information pertaining to the bulk optical properties of near-surface water constituents, including TSS. R_{rs} is defined as the ratio of water-leaving radiance to the downwelling irradiance just above the water and can be related to aquatic reflectance (ρ_w) assuming an isotropic upwelling radiance field, i.e., $R_{rs} = \rho_w/\pi$ (Mobley, 1999). R_{rs} from satellite observations is computed following the removal of atmospheric effects from the top-of-atmosphere (TOA) reflectance/radiance measurements made by remote sensors (Gordon and Wang, 1994). Aquatic biogeochemical products like near-surface concentration of chlorophyll-a (Chl$a$) and TSS together with the inherent optical properties (IOPs) are obtained from R_{rs} products.

Over the last decades, several analytical, empirical, and semi-empirical relationships have been devised to retrieve near-surface TSS (hereafter, TSS) using R_{rs} (or another equivalent representation termed as the normalized water-leaving radiance, nL_w) available at either a single band or a combination of bands (Binding et al., 2010; Dekker et al., 2002; Doxaran et al., 2009a; Han et al., 2016; Nechad et al., 2010; Novoa et al., 2017; Tassan, 1993; Zhang et al., 2016). Site-specific studies often utilize a single red band for TSS retrievals, which can provide reasonably accurate estimates within limited TSS ranges. For example, Ouillon et al. (2004) applied a linear regression analysis to

map TSS within the 0–10 $[g/m^3]$ range in the southwest lagoon of New Caledonia. Similarly, Miller and McKee (2004) estimated TSS in the Mississippi River Delta, where TSS ranged from 0 to 60 $[g/m^3]$. Kumar et al. (2016) and Ondrusek et al. (2012) utilized higher order polynomials to generate spatial distributions of TSS in Chilika Lake, India, (0–100 $[g/m^3]$) and in the Chesapeake Bay (0–60 $[g/m^3]$), respectively. These single band models are easy to implement and straightforward for operational satellite services. However, the performance of these algorithms degrades in areas with extreme sediment loads, where radiometric measurements in the red band no longer correlate with increases in TSS, i.e., a saturation effect is present (Feng et al., 2014; Luo et al., 2018; Ritchie et al., 2003; Shi and Wang, 2009). Under such circumstances, $R_{rs}(\lambda > 700$ nm) is commonly relied upon (e.g., 865, 1020, and 1071 nm) (Knaeps et al., 2015). A major limitation of this NIR-based single band model is that it generally performs poorly for low to moderate TSS (i.e., < 50 $[g/m^3]$) (Han et al., 2016) owing to a) the negligible contribution of particulate backscattering (b_{bp}) relative to the pure water absorption (Doxaran et al., 2012), and b) the lack of radiometric sensitivity in this spectral region. To overcome these limitations, various multiband models based on band ratio or other band-arithmetic operations applied in empirical or semi-analytical models have been developed (Chen et al., 2015; Dekker et al., 2001; Doxaran et al., 2003; Feng et al., 2014; Novoa et al., 2017; Oyama et al., 2009). The main drawback of these methods is that each band is not only sensitive to TSS but also to other optically significant constituents in the water column (e.g., Chl$a$), which leads to overestimation or underestimation of TSS. Alternatively, TSS may be empirically derived from turbidity, a proxy water quality parameter (Dogliotti et al., 2015). Such empirical relationships, though, may vary seasonally due to phytoplankton growth (Hannouche et al., 2017).

In addition to approaches that derive TSS directly from R_{rs}, there are methods that approximate TSS directly from either the particulate absorption coefficient (a_p) (Babin et al., 2003; Zhang et al., 2010; Zheng and DiGiacomo, 2017) or b_{bp} (Binding et al., 2010; Volpe et al., 2011; Woźniak et al., 2010) by estimating mass-specific particulate absorption (a_p^*) and backscattering (b_{bp}^*) coefficients, respectively. Semi-analytical methods that approximate physics-based bio-optical parameterization provide another avenue for TSS retrievals by solving for IOPs. For instance, widely used inversion models such as the Generalized IOP (GIOP) (Werdell et al., 2013), the Quasi Analytical Algorithm (QAA) (Lee et al., 2002), and the Garver-Seigel-Maritorena (GSM) (Maritorena et al., 2002) provide fairly accurate estimates of b_{bp} in clear and/or moderately turbid waters but are less accurate in highly turbid/eutrophic waters (Shanmugam et al., 2010; Zheng and DiGiacomo, 2017). Under intense algal bloom conditions, for example, phytoplankton backscattering dominates $b_{bp}(600$ nm < λ < 800 nm) and, as a result, the corresponding magnitude/shape of R_{rs} (Binding et al., 2010; Shi et al., 2018). This leads to ambiguities in TSS models developed in the absence of high phytoplankton concentrations when they are applied to waters with high concentrations of phytoplankton. Several studies have attempted to fine-tune QAA for IOP retrievals in a few inland and coastal waters (Joshi and D'Sa, 2018; Mitchell et al., 2016; Mouw et al., 2013); nevertheless, these algorithms and their performances require further independent verifications. Most methods neglect impacts of the composition and size-distribution of particles on IOP spectra resulting in inaccurate retrievals of TSS (Bowers and Binding, 2006; Long and Pavelsky, 2013; Neukermans et al., 2012; Novo et al., 1989). Nonetheless, TSS remains a parameter of interest to estimate via remote sensing.

Recognizing the lack of a global dataset for a thorough assessment

of existing TSS algorithms and a robust algorithm applicable to waters with a wide range of near-surface particle load or waters with different particle types, this article offers an innovative hybrid approach termed the <u>S</u>tatistical, <u>I</u>OP-based mu<u>L</u>ti-conditional <u>I</u>nversion proce<u>D</u>ure (SOLID), which employs $b_{bp}(600$ nm $< \lambda < 800$ nm) retrieved from R_{rs} as a proxy for TSS retrievals. The retrieval begins by assigning input R_{rs} to one of three water types according to its shape/magnitude (Section 3). For each of the assigned water types, a corresponding procedure is followed to retrieve b_{bp}. A novel machine learning algorithm is proposed for estimating $b_{bp}(600$ nm $< \lambda < 700$ nm) over a broad range of turbidity and trophic conditions (Section 4.1.1), whereas $b_{bp}(700$ nm $< \lambda < 800$ nm) is analytically solved for in waters mainly dominated by suspended sediments (Section 4.1.2). In aquatic ecosystems (e.g., coastal waters), where low TSS and/or Chl$a$ (i.e., < 2 units of concentrations) is commonly found, QAA is applied for estimating b_{bp} (600 nm $< \lambda < 700$ nm). Then, the retrieved $b_{bp}(600$ nm $< \lambda < 800$ nm) is empirically attributed to TSS via water-type-specific expressions (Section 4.2). The algorithm is developed using a large dataset consisting of synthetic data and *in situ* measurements, and is evaluated with > 2700 paired *in situ* R_{rs} and TSS samples. This approach is further compared against several state-of-the-art algorithms (Miller and McKee, 2004; Nechad et al., 2010; Novoa et al., 2017; Ondrusek et al., 2012; Petus et al., 2010), and is demonstrated for a handful of satellite missions to allow for seamless retrievals of TSS via a single blended algorithm (SOLID). While the performance of the algorithm is mainly demonstrated for the MultiSpectral Instrument (MSI) aboard Sentinel-2A/B, we will further extend our analysis to other satellite missions (Section 5.4), including the Ocean and Land Color Instrument (OLCI), Moderate Resolution Imaging Spectroradiometer (MODIS), Visible Infrared Imaging Radiometer Suite (VIIRS), and Operational Land Imager (OLI) (Section 5.4).

2. Datasets

The data consisted of simulated data (Pahlevan et al., 2017d), *in situ* measurements, and satellite images, representing a broad range of turbidity and trophic conditions. *In situ* measurements (Fig. 1) represented waters with intense algal blooms (e.g., Lake Erie, Lake Champlain, Lake Taihu) and very high turbidity (e.g., Red River and San-Francisco-Bay-Delta Estuary).

These ecosystems represented in the dataset varied in the amount of nutrients, organic matter concentrations, productivity, biodiversity,

Table 1

Summary of statistical attributes associated with *in situ* datasets for training, testing, or validating $b_{bp}(665)$ and TSS retrievals applied for the three water types. Note that the validation dataset is employed for all three water types. See Section 3 for the definition of water types.

	Mean	Median	Max	Min	N
	Training & testing dataset (Type I & II)				
TSS [g/m^3]	14.6	1.94	113.1	0.039	607
Chl$a$ [mg/m^3]	6.11	1.93	161	0.20	460
$b_{bp}(665)$ [1/m][a]	0.17	0.004	2.03	0.0006	607
$R_{rs}(665)$ [1/sr][a]	0.008	0.0071	0.03	0.001	246
	Training & testing dataset (Type III)				
TSS [g/m^3]	150.0	106.8	1190	49.17	112
Chl$a$ [mg/m^3]	10.2	8.1	24.7	1.3	35
$b_{bp}(740)$ [1/m]	1.05	0.67	3.92	0.26	112
$R_{rs}(740)$ [1/sr]	0.019	0.014	0.05	0.006	112
	Validation dataset				
TSS [g/m^3]	30.7	7.94	2626.8	0.102	2729
Chl$a$ [mg/m^3]	19.9	6.52	490	0.02	1916
$R_{rs}(665)$ [1/sr]	0.0103	0.006	0.084	0.001	2729

[a] The band center refers to Sentinel-2A red channel.

climate, and watershed biogeochemical/physical characteristics, which enable a comprehensive assessment of SOLID and other widely used TSS algorithms (Miller and McKee, 2004; Nechad et al., 2010; Novoa et al., 2017; Ondrusek et al., 2012; Petus et al., 2010). These *in situ* datasets include R_{rs} [1/sr] as well as bio-optical and biogeochemical data (Table 1).

2.1. Development data

2.1.1. Synthetic data

The radiative transfer model Hydrolight (Mobley and Sundman, 2008) was used to simulate a large database (*N* = 915,000) of hyperspectral $R_{rs}(350$ nm $< \lambda < 800$ nm) at 5-nm intervals associated with various optical conditions. To do so, various specific absorptions of phytoplankton (a_{ph}^*), specific absorptions/scattering of non-algal particles (a_{nap}^*, b_{nap}^*), particulate backscattering fraction ($\tilde{b}_{bp}$) ($0.01 < \tilde{b}_{bp} < 0.03$) along with vertically uniform Chl$a$ (0.01–100 [mg/ m^3]), TSS (0.0–98.4 [g/m^3]), and the absorption by colored dissolved organic matter $a_{cdom}(440)$ (0.0009–6 [1/m]) with exponents in the range of 0.009–0.031 [1/nm] were supplied as model inputs (Pahlevan
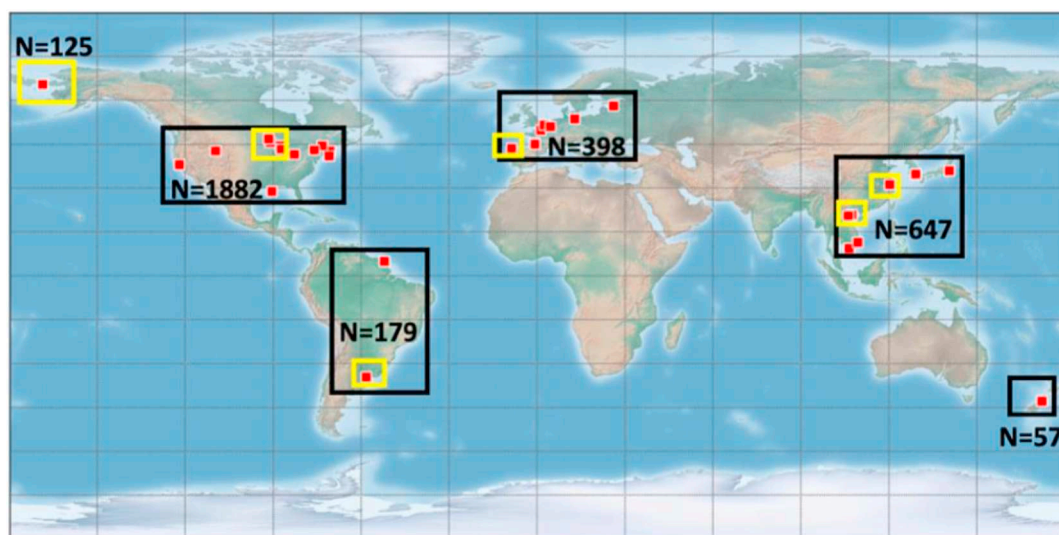
Fig. 1. Global distribution of our *in situ* datasets (*N* = 3288) in addition to the NOMAD datasets (*N* = 222) used for testing, training, and validating the SOLID model. Yellow boxes denote areas with training/testing datasets only, whereas validation data are specified with black boxes. Overall, 2729 independent, paired R_{rs} - TSS measurementes are held for validation (For interpretation of the references to color in this figure legend, the reader is referred to the web version of this article.)

et al., 2017d). The $a_{ph}^*(440)$ ranged from 0.06 to 0.09 [m^2 /mg] while $a_{ph}^*(667)$ varied between 0.02 and 0.06 [m^2 /mg]. For NAP specific absorption and scattering spectra, the five default spectra (e.g., (Bukata et al., 2018)) available via the Hydrolight package were employed. This simulated dataset was used to train a machine learning model for b_{bp} retrievals (Section 4.1.).

2.1.2. Field data

In situ data, such as R_{rs}, b_{bp}, and TSS collected in various inland and coastal waters (Table 1) were compiled. R_{rs} was estimated from measurements made by various above- or in-water radiometers manufactured by Ocean Optics, Inc., Trios, Sea-Bird Scientific, and ASD, Inc. The measurements were post-processed according to instrument-specific protocols and standard procedures developed by the manufacturing companies or the scientific community (Lee et al., 2013; Mobley, 1999; Mueller et al., 2004). Multispectral b_{bp} measurements were taken with ECO BB9 backscattering sensors (WetLabs Inc.; Sea-Bird Scientific). These data, available for narrow spectral bands centered at variable spectral positions (Binding et al., 2019; Moore et al., 2017; Mouw et al., 2013; Reynolds et al., 2016), were linearly over-sampled to 1-nm spectral spacing for a subsequent resampling to corresponding satellite sensor spectral response functions (see Section 4.1.2). Overall, 246 pairs of R_{rs} and b_{bp} spectra were available to validate b_{bp} estimates within the visible spectrum (Tables 4 and A1). TSS was determined gravimetrically using the standard technique and represent the dry mass particles per unit volume of water. *In situ* TSS - b_{bp} measurement pairs ($N = 607$) were further utilized to develop empirical relationships for TSS retrievals (Table 1). The data originated from Lake Erie, Green Bay (WI), Lake Michigan (MI) from U.S. inland waters ($N = 150$), Lake Taihu ($N = 164$) in China (Shi et al., 2018), and the SeaWiFS Bio-optical Archive and Storage System (SeaBASS) ($N = 293$). In sediment-rich waters (where TSS is commonly > 60 [g/m^3]), we applied all available R_{rs} and TSS data ($N = 112$), acquired in European waters (Knaeps et al., 2018) ($N = 78$) and in the Red River ($N = 34$), Vietnam (Pham et al., 2018).

For validating the TSS retrievals, a large independent database ($N = 2729$) of R_{rs} – TSS measurements, whose frequency distributions are illustrated in histograms in Fig. 2, were applied. These datasets were collected in various open ocean/coastal/inland regions over the globe, such as Río de La Plata and French Guiana (South America), the Gulf of Mexico, the San-Francisco-Bay-Delta Estuary, Chesapeake Bay, and the Plum Island Estuary (North America), the south Atlantic Bight, the English Channel and French nearshore coastal waters, the Estonian inland waters and Baltic Sea (Europe), coastal waters of South Korea, lakes in New Zealand, and inland and bay waters of Vietnam (Asia) (Fig. 1). In addition, we used a subset of data available in the NASA bio-Optical Marine Algorithm Dataset (NOMAD) (Werdell and Bailey, 2005).

2.2. Image data

Optical remote sensing images over select coastal and inland waters from the MSI were obtained from the United States Geological Survey (USGS) image portal (https://earthexplorer.usgs.gov/) and processed to R_{rs} using the SeaWiFS Data Analysis System (SeaDAS v7.5.3) with the 1609–2200 nm band combination for aerosol removal (Pahlevan et al., 2017b; Pahlevan et al., 2017c) to allow for the use of 865 nm for TSS retrievals in highly turbid waters. To extend the performance analysis in extremely turbid waters, MSI images were also processed using ACOLITE (v20190326.0), which is commonly used in such environments (Vanhellemont and Ruddick, 2014). Corrected images were processed to TSS fields for assessment of realistic spatio-temporal patterns according to expert expectations.

3. Water-type classification

Following Novoa et al. (2017) and our objective to devise an algorithm applicable to a broad range of TSS, we conducted a simple water-type classification using available *in situ* R_{rs} spectra. We classified waterbodies into three basic types determined by the shape of R_{rs}. The classification rules, designed experimentally following trials and errors, are summarized in Table 2.

These rules are applied in hierarchical order (e.g., input spectrum is first examined for its assignment to Type II; if the condition is not met then the spectrum is assessed for Type III). The classification scheme is primarily based upon three bands (blue, green, and red) to assure its utility for heritage Landsat-class missions not equipped with red-edge bands. The three broad categories include: Blue-green waters (Type I); R_{rs} falling into this category commonly exhibit very low magnitudes within the red region, i.e., $R_{rs}(560) < R_{rs}(492)$. These are normally optically mixed waters with no single dominant water constituent. In clearer waters, R_{rs} is characterized with peaks in the blue region whereas in more turbid waters a peak in the blue-green region commonly exists (Fig. 3) — Green waters (Type II); The characteristic peak in R_{rs} for these water types is within the green region due to the elevated total absorptions in the blue and red portions of the spectrum (Fig. 3). In these water types, the presence of CDOM further increases absorption within the blue region lowering upwelling radiance compared to that in the red, i.e., $R_{rs}(665) > R_{rs}(492)$ — Brown waters (Type III); The primary peak in R_{rs} is shifted to the red region i.e., $R_{rs}(665) > R_{rs}(\lambda)$. Here, the magnitude of R_{rs} in the red region is almost always greater than those in the blue and green regions. This enhanced response is mainly because of the increased backscattering in presence of sediments or non-algal particles, as well as the dampening effects of CDOM at lower wavelengths (Schalles, 2006). These spectral features are expected in river runoffs, estuaries, and bays with significant sediment loads (Doxaran et al., 2003; Gernez et al., 2014) (Fig. 3). Further analysis of R_{rs} spectra suggested the need for an additional criterion to enhance discrimination of water types II and III.

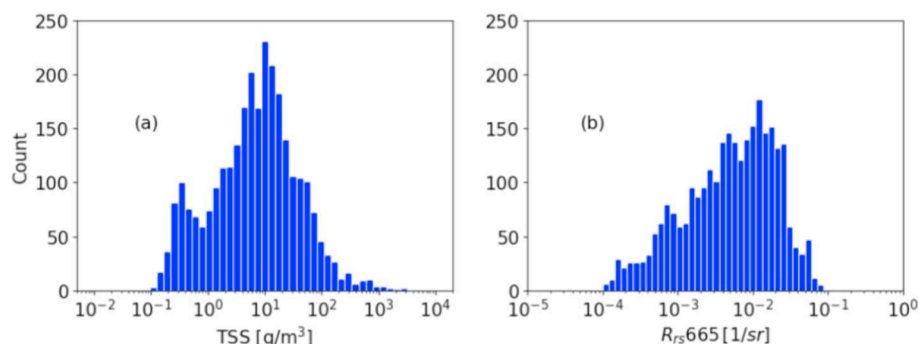The misclassification arises from enhanced backscatter in the

Fig. 2. Frequency distribution of validation dataset ($N = 2729$): TSS (a) and R_{rs} (665) (b).

Table 2
Classification rules for water type determination.

Order	Rule	Class
1	If $R_{rs}(665) < R_{rs}(560)$ & $R_{rs}(665) > R_{rs}(492)$	$R_{rs}(\lambda) \in$ Type II
2	If $R_{rs}(665) > R_{rs}(560)$ & $R_{rs}(740) > 0.01$ [1/sr]	$R_{rs}(\lambda) \in$ Type III
3	If $R_{rs}(560) < R_{rs}(492)$	$R_{rs}(\lambda) \in$ Type I
4	If #3 is false	$R_{rs}(\lambda) \in$ Type II

vicinity of 740-nm channel in hypereutrophic waters (Gitelson et al., 2008). Hence, another condition, i.e., $R_{rs}(740) > 0.01$ [1/sr], was added to avert this misclassification. Given our paired R_{rs} and TSS dataset, TSS > 65 [g/m^3] commonly falls in Type III category.

4. Methodology

The methodology followed in this study is explained below in two main steps: (a) deriving b_{bp} from R_{rs}, and (b) estimating TSS from b_{bp}. The schematic diagram is shown in Fig. 3. Recognizing that commonly used IOP retrieval algorithms are designed to function in oceanic waters

(Werdell et al., 2018), we devise new approaches for b_{bp} retrievals in Type II and Type III waters. For Type I waters, following our performance assessments (Section 5.1), QAA was chosen to approximate b_{bp}.

4.1. b_{bp} inversion

In situ measured R_{rs} data available in this study can be expressed as the subsurface remote sensing reflectance (r_{rs}) by accounting for air-water transmittance as below (Lee et al., 2002):

$$r_{rs} = \frac{R_{rs}}{0.52 + 1.7 R_{rs}} \tag{1}$$

This quantity is analytically related to the ratio of total backscattering (b_b) to the sum of b_b and total absorption (a) (Gordon et al., 1988; Lee et al., 2002). Using the constant model parameters ($g_1 = 0.0949$ and $g_2 = 0.0794$), the relationship can be expressed as follows:

$$r_{rs}(\lambda) \approx g_1 \left(\frac{b_b(\lambda)}{a(\lambda) + b_b(\lambda)} \right) + g_2 \left(\frac{b_b(\lambda)}{a(\lambda) + b_b(\lambda)} \right)^2 \tag{2}$$

where a and b_b can be further decomposed into:

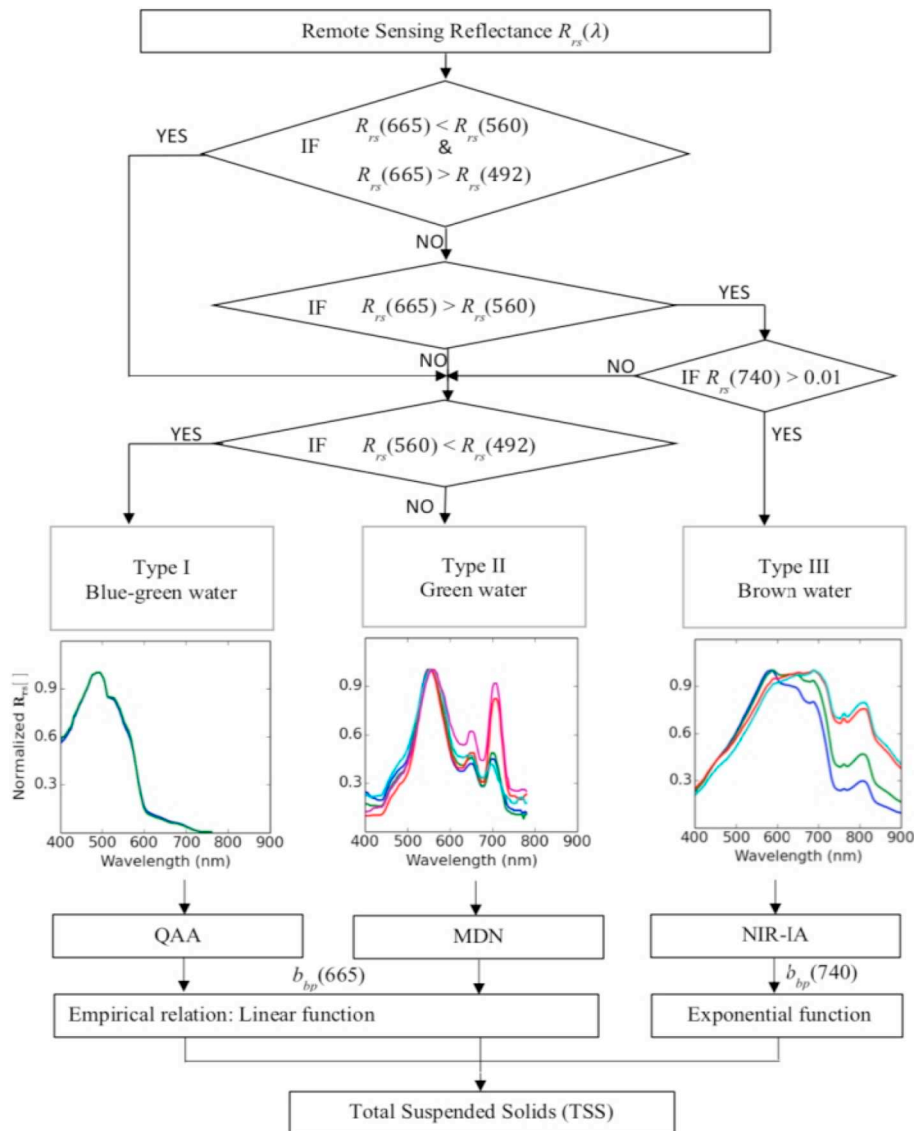**Fig. 3.** Flowchart showing the sequence of our hybrid retrieval strategy (i.e., SOLID). The input spectrum is first assigned to a water type followed by applying b_{bp} retrieval algorithms, i.e., the Quasi Analytical Algorithm (QAA), the Mixture Density Network (MDN), and a NIR-based Inversion Approach (NIR−IA). The TSS is then estimated from b_{bp} using empirical relationships. Input R_{rs} is normalized by the peak value.

$$a(\lambda) = a_{\mathrm{w}}(\lambda) + a_{\mathrm{ph}}(\lambda) + a_{\mathrm{cdom}}(\lambda) + a_{\mathrm{nap}}(\lambda) \qquad (3)$$

$$b_{\mathrm{b}}(\lambda) = b_{\mathrm{bw}}(\lambda) + b_{\mathrm{bp}}(\lambda) \qquad (4)$$

In above equations, a_{w} is the pure water absorption (Pope and Fry, 1997), a_{ph} stands for phytoplankton absorption, and a_{nap} represents absorption due to non-algal particles. Similarly, b_{b} includes b_{bw}, the pure water backscattering — half of the pure water scattering ($b_w/2$) (Smith and Baker, 1978) — and b_{bp} is the particulate backscattering due to algal and non-algal constituents. These fundamentals will be referenced when deriving b_{bp} for Type III waters in Section 4.1.2.

4.1.1. Machine learning approach: mixture density network

In the past, artificial neural networks have been relied upon for component IOP inversions in optically complex waters (D'Alimonte et al., 2012; Ioannou et al., 2011). Here, for Type II waters, using the synthetic data described in Section 2.1, we train a machine learning model termed the Mixture Density Network (MDN) for b_{bp} retrievals (Section 3 and Table 1). This model has recently shown promise in retrieving Chl$a$ from multispectral images (Pahlevan et al., 2020). MDNs are a class of neural networks for modeling a mixture of Gaussian functions (Bishop, 1994). Instead of directly outputting the target variable (e.g., b_{bp}), this network generates a set of three variables per Gaussian (mean, standard deviation, and mixing coefficients), where the number of Gaussians is a tuning parameter. The Gaussians are then combined to form the final output estimation, via either a probabilistic combination, or the maximum likelihood. MDNs are intended to model a Y to X mapping; that is, in contrast to many standard machine learning models, whose main intent is to find a function mapping X to Y. The primary difference between the two is that in the latter case, there may be many X values for any particular Y value (e.g. a sine wave). In the former case, modeled by an MDN, the situation is reversed: there may be many Y values for any particular X value (e.g., an arcsine wave). The implemented MDN model learns the full covariance matrix formed of b_{bp} spectrum, avoiding ambiguities in retrievals (Sydor et al., 2004; Yang et al., 2011). To state this another way, a given R_{rs} value for an arbitrary channel may be consistent with multiple different possible b_{bp} values; without more spectral information, the probability of all of these values are potentially equal. A standard machine learning model may, in the worst case, simply take the average of all these disparate values. The MDN, however, learns to associate the

R_{rs} spectrum with multiple parameters; thus, enabling a choice of a b_{bp} spectrum, which is more likely, conditional upon all spectral bands. A schematic diagram of the model is shown in Fig. 4.

Input to the model consists solely of the R_{rs} spectra, which are normalized based on median centering and interquartile scaling. The learned output variables are subject to the same scaling method, but also subsequently scaled to a [0.1, 1] range. This normalization method is robust to outliers which may be present in the data, while also bringing network outputs into a range, which is amenable to activation functions, such as rectified linear units (ReLU); thus, helping to avoid the dying ReLU problem (Agarap, 2018). The output of the model consists of b_{bp} spectra.

There are a number of hyperparameters to tune, including the number of Gaussian distributions which are modeled, the Gaussian mixing coefficients, as well as all standard neural network hyperparameters. These choices appear to be fairly robust to changes within the current implementation, especially with regard to the MDN-specific options. The current default model uses a five-layer neural network with 25 neurons per layer, which is trained to output the parameters of five Gaussians. From this mixture model, the overall estimate is selected via the Gaussian with the maximum prior likelihood. The described model is trained a number of times with random initializations of the underlying neural network, in order to ensure a stable final output of the estimates. The median estimate is taken as the final result of these trials, with convergence occurring within some small margin of error after approximately ten trials. Note that none of these values are required at test time – they are used as output variables, and so are produced by the model. The only input variables required are the R_{rs} values at five different bands (443, 492, 560, 665, 705 nm).

4.1.2. NIR-based inversion approach (NIR-IA)

For Type III waters, due to the absence of available in situ b_{bp} ($\lambda > 700$ nm) driven by saturation effects associated with backscattering sensors (Doxaran et al., 2016), we adopt a different strategy. Applying the component models to Eqs.(1)–(4), a modeled R_{rs} spectrum for a NIR band of MSI can be constructed as

$$R_{rs}(740) = (f/Q)\frac{b_{\mathrm{bw}}(740) + b_{\mathrm{bp}}(740)}{a_{\mathrm{w}}(740) + a_{\mathrm{nap}}(740) + b_{\mathrm{bw}}(740) + b_{\mathrm{bp}}(740)} \qquad (5)$$

Here, $a_{\mathrm{w}}(740) = 2.72$ [1/m] (Pope and Fry, 1997) and $b_{\mathrm{bw}}(740) =$
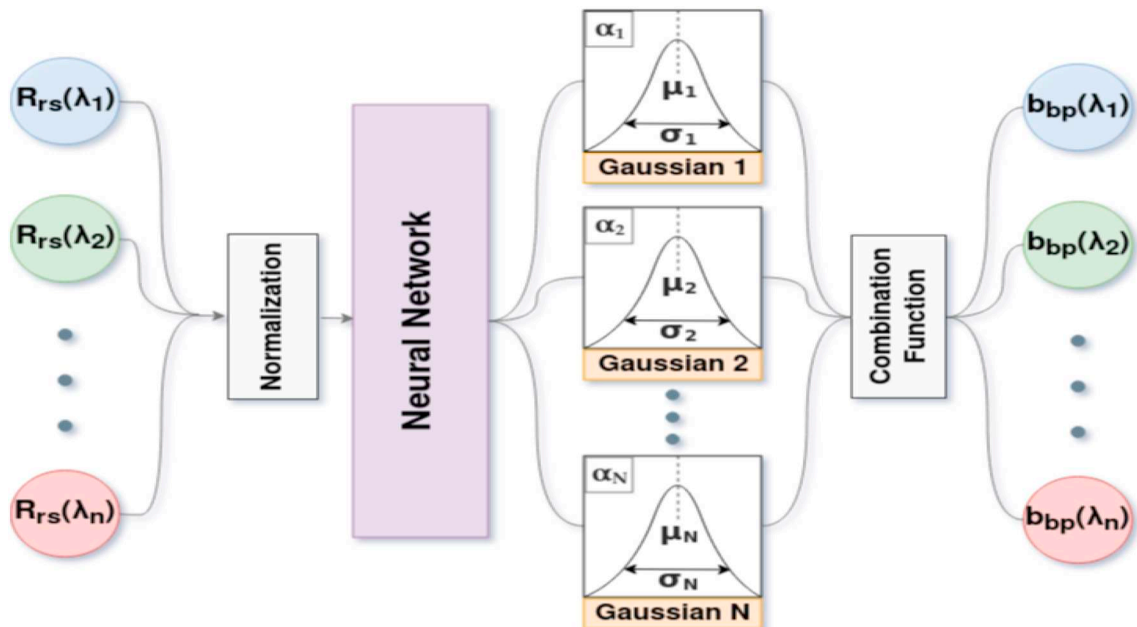

Fig. 4. Block diagram of the MDN network used for the retrieval of particulate backscattering (b_{bp}) from R_{rs} for Type II waters.

0.00026 [1/m] (Smith and Baker, 1978) are the pure water absorption and backscattering coefficients, and the f/Q factor is assumed constant, i.e., 0.105 (Morel and Prieur, 1977), although variability in f/Q does exist in coastal and inland waters (Loisel and Morel, 2001; Morel et al., 1995). According to the literature (Babin and Stramski, 2004; Doxaran et al., 2009b; Estapa et al., 2012), we adopted $a_{nap}^*(740) = 0.011 [m^2/g]$, which gives rise to $a_{nap}(740) = 1.50$ [1/m] given the mean TSS value of 150 [g/m^3] for our dataset (Table 1). Under these assumptions, $b_{bp}(740)$ can be obtained by re-arranging the above equation. The discussion on the uncertainties introduced via this assumption is provided in Section 6.1. The band centers of the relative spectral response (RSR) functions used for b_{bp} retrievals for all the satellite missions considered here are summarized in Table 3. For Landsat-class missions, where a 740-nm channel is absent, we develop a very similar approach applicable to the 865-nm channel. A power-law model fitted to the global statistics corresponding to an average a_{nap}^* spectrum (see Table 5 in Doxaran et al. (2009b)) was employed to extrapolate $a_{nap}^*(740)$ to 865 nm channel. This extrapolation resulted in $a_{nap}(865) = 0.55$. Together with $a_w(865) = 4.6$ [1/m] and $b_{bw}(740) = 0.00014$ [1/m], Eq. (5) was solved for $b_{bp}(865)$.

4.2. TSS retrieval

With the knowledge of b_{bp}, we construct an empirical model to obtain TSS estimates applicable to both Type I and II waters, and one model for Type III. We found a strong power-law correlation ($R^2 = 0.97$) between $b_{bp}(665)$ and TSS in both Type I and II waters from Lake Erie (N = 150; with $0.13 < TSS < 43.1$ [g/m^3] and $0.2 < Chla < 57$ [mg/m^3]). Fig. 5a illustrates this strong correlation on a log-log plot. The regression equation is as follows:

$$TSS = 53.736 \times b_{bp}(665)^{0.8559} \tag{6}$$

To affirm this relationship for a wider dynamic range, additional paired $b_{bp}(665)$ and TSS data from highly productive waters of Lake Taihu (N = 164, Shi et al., 2018), the Arctic region (N = 125, (Reynolds et al., 2016)), and U.S. coastal waters (Casey, 2019; Wei et al., 2016) were applied. The data overlaid onto Fig. 5a further indicate that the relationship, to a large extent, holds ($R^2 = 0.82$) in intense algal bloom conditions (Type II).

In Type III waters, TSS was estimated via $b_{bp}(740)$, which is derived directly from *in situ* measured $R_{rs}(740)$ (Section 4.1.2.; Eq. (5)) using SEASWIR data (N = 78) (Knaeps et al., 2018) in sediment-rich waters (i.e., Scheldt River, Gironde River, Rio de La Plata). Fig. 6b shows the (log-log) scatterplot for the derived TSS - $b_{bp}(740)$ relationship demonstrating a fairly strong relationship, i.e., $R^2 = 0.83$, expressed as follows:

$$TSS = (207.57 \times b_{bp}(740)) - 46.78 \tag{7}$$

This least square fit suggests the utility of this relationship for a wide range of TSS and $b_{bp}(740)$ from 65–1300 [g/m^3] and from 0.3 to 5.0 [1/m], respectively. In order to further corroborate this relationship, another dataset (N = 34) from highly turbid waters ($13.6 < TSS < 178.3$ [g/m^3]) of the Red River, Vietnam, are overlaid onto the scatterplot (Fig. 5b). Adding these data left R^2 unchanged, indicating robustness of the model to different hydro-geomorphological conditions. Note that $b_{bp}(740)$ was similarly derived from $R_{rs}(740)$ for this dataset. Analogously, we developed a relationship for TSS retrievals from $b_{bp}(865)$ for OLI (Section 4.1.2; Fig. A.1)

$$TSS = (224.43 \times b_{bp}(865)) - 12.575 \tag{8}$$

It should be further noted that due to the absence of a NIR channel in the 740-nm region among the OLI suite of measurements, the corresponding conditional rule for Type III waters (Table 2) cannot be evaluated; hence, elevated uncertainties are expected.

In summary (Fig. 3), to perform TSS retrievals, SOLID selects b_{bp} inversion models according to a select water type. For Type I and II

Table 3
Band centers (nm) of RSR functions of satellite mission considered in this study.

	MSI	VIIRS	MODIS	OLCI	OLI
Type I	665	672	667	665	655
Type II	665	672	667	665	655
Type III	740	748	748	754	865

waters, where QAA and MDN are utilized, SOLID applies Eq. (6) where TSS is expected to be within the 0.1–65 [g/m^3] range. In extremely turbid waters (Type III), SOLID uses the NIR-based Inversion Approach (NIR-IA) followed by Eq. (7) or Eq. (8) for TSS estimations. The analysis presented in Section 5 reflects the performance of SOLID v1.0, whose underlying MDN model has been updated as part of SOLID v2.0.[1]

4.3. Performance metrics

In this study, we examine both linear and log-transformed metrics for evaluations of estimated (E) quantities (b_{bp} or TSS) against those measured (M) *in situ*. The evaluation of all TSS algorithms is carried out using an in situ validation set (N > 2700) independent of the training set. The performance metrics are as follows

$$RMSE = \left[\frac{\sum_{i=1}^{N} (\log_{10}(E_i) - \log_{10}(M_i))^2}{n} \right]^{1/2} \tag{9}$$

$$MAPE = 100 \times median [|E_i - M_i|/M_i] \text{ for } i = 1, ..., N \tag{10}$$

$$Bias = 10^Z \text{ where } Z = \left[\sum_{i=1}^{n} (log_{10}(E_i) - log_{10}(M_i))/N \right] \tag{11}$$

$$MAE = 10^Y \text{ where } Y = \left[\sum_{i=1}^{n} |log_{10}(E_i) - log_{10}(M_i)|/N \right] \tag{12}$$

where RMSE is the root mean squared logarithmic error, MAPE is the median absolute percentage error, Bias represents log-transformed residuals, and MAE stands for the mean absolute error computed in log-space. The metrics computed in log-transformed space are believed to provide a better assessment of the algorithms owing to the log-normal distribution of TSS data (Fig. 2). The interpretation of Bias and MAE are as follows: Bias of 1.5 or 0.8 implies that TSS estimations are 50% and 20% overestimated or underestimated, respectively. Similarly, MAE of 1.2 suggests 20% overall error; however, MAE takes on values equal to or greater than unity and is a very robust metric to gauge the overall performance of an algorithm. In addition to the above metrics, we will also include slope associated with the linear regression fits to facilitate comparisons with previous publications.

5. Results

The results are presented in four subsections. First, an assessment of b_{bp} inversion is presented. This is followed by a full evaluation of the SOLID model and comparing it against five existing algorithms. TSS maps generated from 13 MSI images are then qualitatively examined. Lastly, the performance assessment is extended to OLCI, MODIS, VIIRS, and OLI to demonstrate the utility of SOLID for multimission production of TSS products.

5.1. b_{bp} retrievals

To choose an appropriate $b_{bp}(665)$ retrieval method, we compared the performances of our inversion techniques with those of widely used

---

[1] The source code can be accessed via https://github.com/BrandonSmithJ/MDN/tree/master/Benchmarks/tss/SOLID.
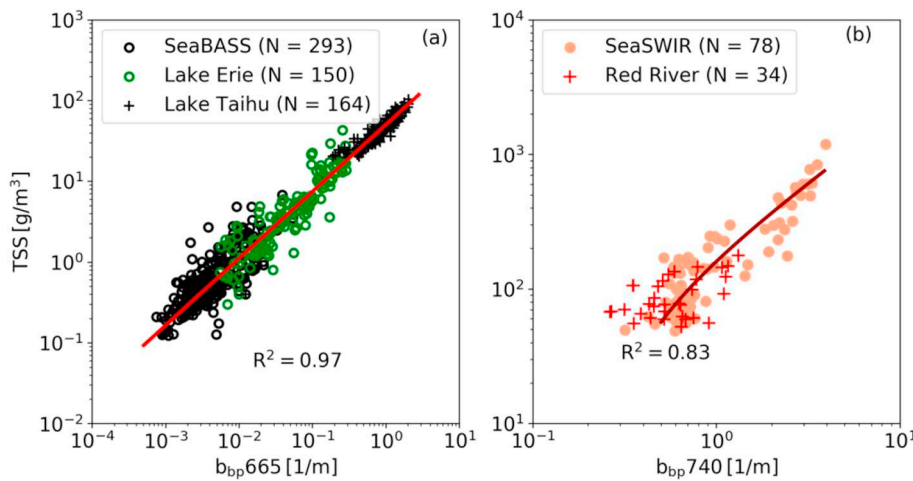
Fig. 5. (a) A power-law function ($R^2 = 0.97$) for TSS - b_{bp}(665) in Type I (blue-green) and Type II (green) waters ($n = 607$). **(b)** Scatterplot corresponding to *in situ* TSS and b_{bp}(740) (derived from R_{rs} (740) using Eq. 5) datasets ($N = 112$) collected in sediment-dominated waters (Type III). Note that the fitted lines are displayed in log-log scale. (For interpretation of the references to color in this figure legend, the reader is referred to the web version of this article.)
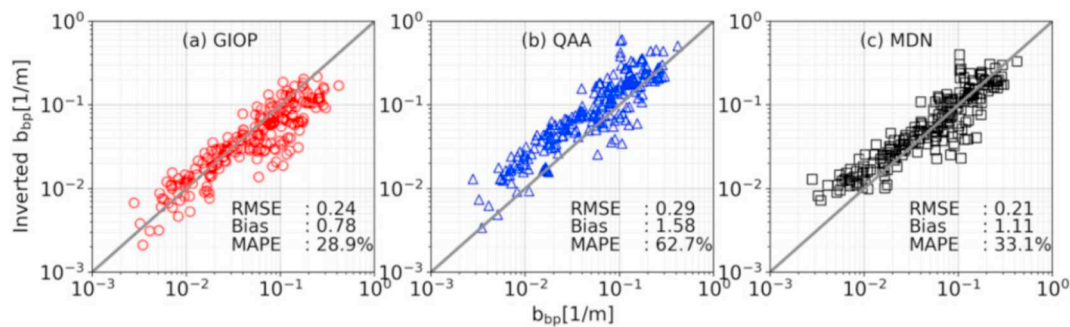

Fig. 6. Comparison of the modeled (y axis) and *in situ* measured b_{bp}(665) from GIOP, QAA, and MDN for Type II waters (N = 211); see Table 4 for accompanying statistics.

state-of-the-art IOP algorithms, namely QAA (Lee et al., 2002) and the GIOP (Werdell et al., 2013) with its default configuration. For Type I waters, given a small validation sample size ($N = 35$), we found that QAA provides better b_{bp}(665) retrievals than GIOP (Table 4). Our statistical attributes, however, confirm that both QAA and MDN are proper candidates with QAA showing a better performance according to MAPE and slope while MDN provides superior estimates given MAE and RMSE. Consequently, there was no strong evidence to choose one over the other, likely owing to the lack of representative validation data. We, therefore, decided to choose the better approach via appraising TSS retrievals (Section 5.2). Our analysis suggested that QAA yields more accurate retrievals of TSS ($N = 430$) and, as a result, better b_{bp}(665) in Type I waters (Table 4).

As illustrated in Fig. 6, the performance of MDN for Type II waters was also benchmarked against those of QAA and GIOP (Table 4) using *in situ* b_{bp}(665) ranging from 0.05 to 0.5 [1/m] ($N = 211$; mean of 0.069, median of 0.041, and standard deviation of 0.072). Both GIOP and QAA approximate b_{bp}(665) with relatively large biases and RMSEs, exceeding those of MDN (e.g., QAA returns overestimated quantities). Overall, the MDN produces better results than these two state-of-the-art algorithms, albeit GIOP is a competitive algorithm in such eutrophic waters (Figs. 3 and 5). The fairly low Bias and RMSE (i.e., 0.21) together with a slope close to unity are evidence for its strong performance for a wide range of b_{bp}(665) in Type II waters. Note that MDN produces fairly robust b_{bp} across the rest of the visible bands in Type II waters. The performance assessment associated with the four visible MSI bands is summarized in Table A1 (Appendix A). Due to their intended design targeting robust retrievals in clear ocean waters (Mitchell et al., 2016; Wang et al., 2009; Zheng et al., 2014), QAA and GIOP are expected to have limited use in Type III waters (Section 1). Hence, we adopted our NIR-IA, developed using published *in situ* data (Knaeps

et al., 2018), as the optimal approach for estimating b_{bp}(740).

5.2. TSS validation

Here, the performance of the state-of-the-art TSS models (Miller and McKee, 2004; Nechad et al., 2010; Novoa et al., 2017; Ondrusek et al., 2012; Petus et al., 2010) is compared against that of SOLID (see Table A2 for expressions). Fig. 7 shows the performances of these models using an independent *in situ* dataset ($N = 2729$; Table 1). The Miller model (Fig. 7a) shows a fair performance in Type II waters, while it performs poorly in Type III waters and produces negative TSS values in

Table 4
The performance of GIOP, QAA, and MDN as compared to *in situ* b_{bp}(665). The NIR-IA retrievals were not assessed due to the absence of *in situ* b_{bp}(740). Global statistics are associated with all Type I and Type II data. Best statistical attributes in each category are boldfaced.

Model	MAPE [%]	MAE	RMSE	Slope	Bias[a]	N
			Global			
GIOP	33.2	1.58	0.26	**0.98**	0.74	246
QAA	57.7	1.74	0.29	1.04	1.44	
MDN	**32.4**	**1.47**	**0.22**	0.93	**1.07**	
			Type I			
GIOP	39.37	1.97	0.38	1.03	0.52	35
QAA	**21.58**	1.57	0.29	**1.02**	**0.85**	
MDN	31.63	**1.49**	**0.24**	0.75	0.85	
			Type II			
GIOP	**28.94**	1.52	0.24	0.85	0.78	211
QAA	62.70	1.76	0.29	**0.90**	1.58	
MDN	33.15	**1.47**	**0.21**	0.85	**1.11**	

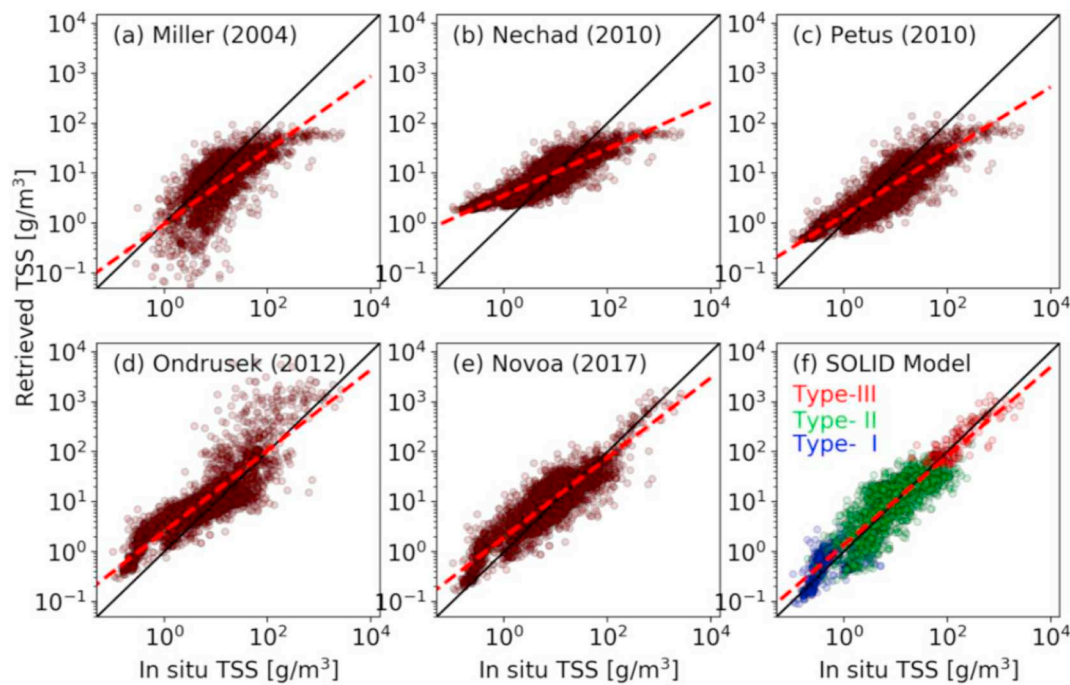[a] Bias = 1 is considered ideal (zero-bias) – see Eq. (11).

Fig. 7. Performance evaluation of multiple TSS retrieval methods shown alongside SOLID (f) applied to simulated MSI spectral bands. An independent *in situ* dataset (N = 2729) was utilized. The benchmark algorithms are (Miller and McKee, 2004) (a), (Nechad et al., 2010) (b), (Petus et al., 2010) (c), (Ondrusek et al., 2012) (d), and (Novoa et al., 2017) (e).

Type I waters. Using $R_{rs}(665)$, the Nechad model (Fig. 7b) performs well in Type II waters, contrasted with its poor performance in Type I and III waters. The Petus model retrieves TSS values better than the Nechad model for Type I waters and exhibits slightly poorer performance in Type II waters (Fig. 7c). From Fig. 7a, b, c, it is evident that R_{rs} (665) tends to saturate for TSS > 50 [g/m³] (Doxaran et al., 2014; Feng et al., 2014; Han et al., 2016; Shi and Wang, 2009). The Ondrusek model (Fig. 7d) surmounts the saturation effect (non-linearity) via a 3rd order polynomial fit, with $R_{rs}(640)$ as the independent variable. Yet, the TSS estimates via this model are largely overestimated for all the three types (Fig. 7d). Note, however, that, in this study, $R_{rs}(665)$ was supplied to this model. The Novoa model clearly shows robust retrievals (Fig. 7e) across all water types compared to the other existing models. That said, according to the global statistics provided in Table 5, SOLID outperforms all the state-of-the-art models by a large margin (Table 5; Fig. 7f). The improvements made possible by SOLID compared to second and third best models, i.e., Novoa and Nechad, are 10–20% in MAPE, 6–30% in MAE, 10–43% in RMSE, and 15% in Bias and slope. The one-to-one agreement with significantly small errors across this wide dynamic range (0.10 < TSS < 2626.8 g/m³) suggests that SOLID has the potential for producing reasonably accurate/precise TSS products at global scales in coastal and inland waters.

The water-type-specific performance statistics are elaborated upon in Table 5. It can be inferred that, in blue-green waters, SOLID significantly outperforms all the state-of-the-art algorithms, suggesting its viability for moderately turbid coastal waters. For Type II waters, the performance of SOLID closely resembles those of Nechad and Novoa. The main difference stems from near-zero bias and near-unity slope that renders SOLID superior. Further, SOLID exhibits a notably better performance than the rest of the models in Type III waters. The second-best model is the Novoa model, which exhibits comparable MAPE to that of SOLID, but performs less well when other metrics are examined. It should be noted that the performances of three other models (Han et al., 2016; Siswanto et al., 2011; Zhang et al., 2010) were also examined. Of these, the models by Siswanto et al. (2011) and Zhang et al. (2010) performed poorly for the full range of TSS. On the other hand, the

Table 5

Statistical analysis of TSS retrievals from existing algorithms and our proposed approach (SOLID) using a comprehensive in situ dataset for different types of water. Note that negative retrievals by the Miller model were excluded from calculations. The statistical characteristics for SOLID are boldfaced. The negative retrievals of the Miller model in Type I and II waters are excluded from statistical computations.

TSS Model	MAPE [%]	MAE	RMSE	Slope	Bias[a]	N
			Global			
SOLID	**48.94**	**1.81**	**0.32**	**0.97**	**1.09**	2729
Miller	58.82	2.56	0.53	1.05	0.50	2152
Nechad	59.74	2.31	0.46	0.53	1.26	2729
Petus	57.71	2.17	0.41	0.72	0.70	
Ondrusek	68.38	2.28	0.46	0.90	1.60	
Novoa	52.73	1.92	0.35	0.84	1.27	
			Type I			
SOLID	**52.86**	**1.76**	**0.31**	**0.93**	**1.14**	430
Miller	49.37	2.80	0.60	1.49	0.49	44
Nechad	544.92	5.23	0.77	0.32	5.12	430
Petus	110.33	2.20	0.37	0.52	1.73	
Ondrusek	233.15	3.36	0.58	0.89	3.21	
Novoa	95.66	2.29	0.42	0.98	1.96	
			Type II			
SOLID	**50.15**	**1.86**	**0.33**	**0.98**	**1.09**	2122
Miller	57.10	2.43	0.51	1.24	0.54	1931
Nechad	50.48	1.87	0.33	0.64	1.08	2122
Petus	50.99	2.05	0.38	0.84	0.64	
Ondrusek	55.95	2.08	0.42	0.95	1.38	
Novoa	50.08	1.87	0.34	0.83	1.22	
			Type III			
SOLID	**31.41**	**1.48**	**0.22**	**0.86**	**1.02**	177
Miller	73.94	4.43	0.73	0.40	0.23	
Nechad	71.44	4.09	0.70	0.37	0.24	
Petus	73.37	4.29	0.71	0.53	0.23	
Ondrusek	73.74	2.64	0.54	1.37	1.71	
Novoa	33.21	1.72	0.34	1.17	0.73	

[a] Bias = 1 is considered ideal (zero-bias) – see Eq. (11).

model of Han et al. (2016) performed fairly well in Type II waters but exhibited saturations in Type III waters.

5.3. Applications to Sentinel-2 imagery

For demonstration purposes, several satellite images with a wide range of optical regimes were processed. The goal is to ensure that the model is capable of producing reasonable spatial distribution maps according to expert expectations; therefore, the absolute retrievals are not examined due to the absence of reliable *in situ* matchups. Multiple cloud-free images over the Chesapeake Bay (MD, USA), San-Francisco-Bay Delta Estuary (CA, USA), Lake Okeechobee (FL, USA), and Lake Taihu (China) were selected to assess spatial distributions of TSS. Fig. 8 demonstrates ACOLITE-processed MSI-derived TSS products (29th Aug 2018, 27th December 2018, 25th February 2019, and 6th April 2019) obtained from SOLID, the Ondrusek model (Ondrusek et al., 2012), and the Nechad model (Nechad et al., 2010) in the upper Chesapeake Bay area. This region is recognized for its high spatio-temporal variability in

sediment loads due to tidal forcing and freshwater inputs from different watersheds (Fugate et al., 2007; Kemp et al., 2005; Ondrusek et al., 2012). High sediment loads along with bio-optical variability in CDOM and Chl*a* pose challenges in TSS retrievals in this region (Aurin and Dierssen, 2012; Werdell et al., 2010). The TSS variability obtained from the SOLID model over different seasons was closely matched with the regional maps produced by the Ondrusek model, specifically designed for the Chesapeake Bay. Similar variabilities are not captured in the products created via the Nechad model, which is expected to fail to retrieve high TSS values in the upper Chesapeake Bay area (Fig. 7b). Although there are discrepancies in the absolute values, the relative spatial distributions of the two products, in particular, in the northern sections of the bay resemble that of the SOLID model, which is expected to produce more accurate concentrations (Fig. 6 and Table 5), i.e., the Ondrusek model tends to overestimate TSS and Nechad model is saturated (Fig. 7b & d). Additionally, it is worth noting that the SOLID model produces smooth transitions between the three water types (regions) and no artifacts are introduced as a result of the water-type
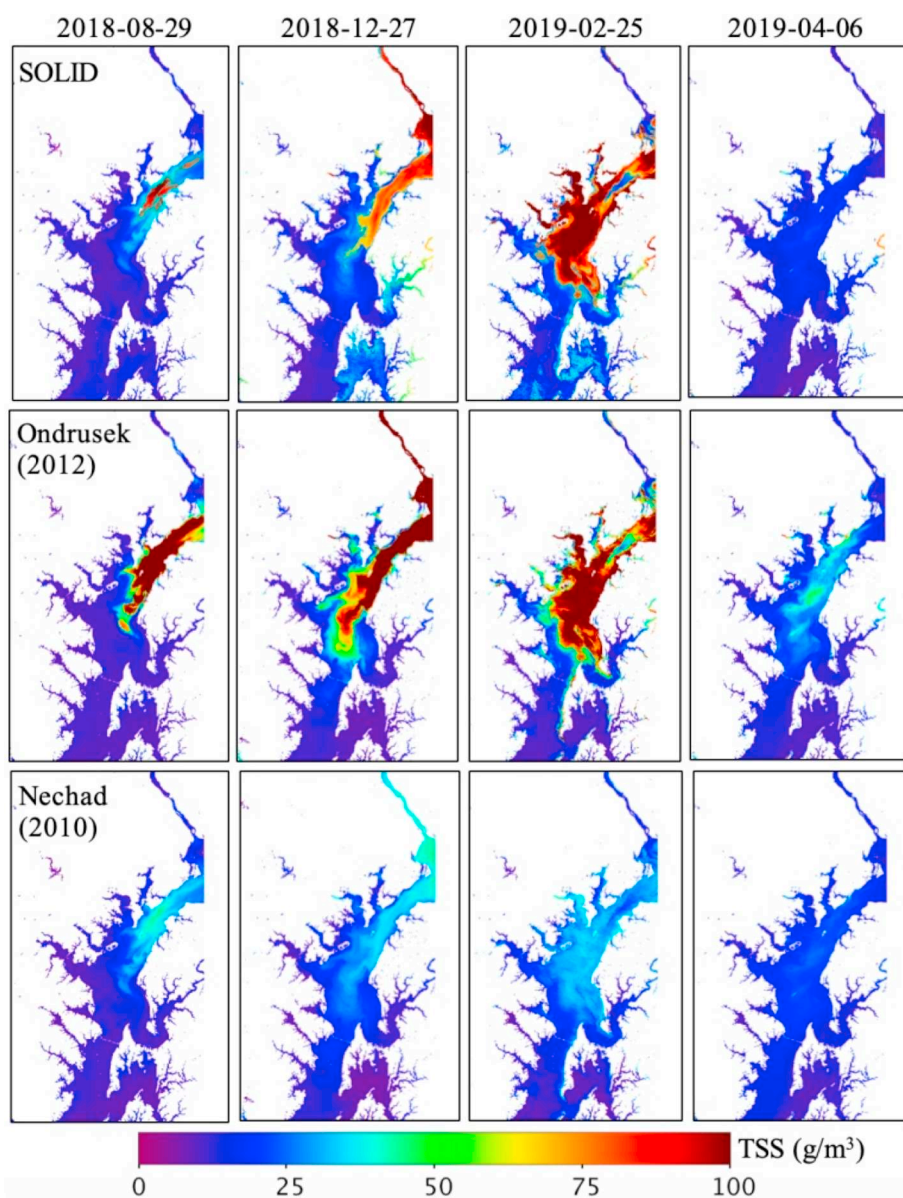

Fig. 8. ACOLITE processed MSI-A images show the spatial distribution of TSS over the Chesapeake Bay in 2018 (29th August and 27th December) and 2019 (25th February and 6th April). (Top row) TSS retrieved from the SOLID model, (Middle row) from a regional model (Ondrusek et al., 2012), and (Bottom row) from the Nechad model (Nechad et al., 2010). See Fig. A.2 for maps of water-types.

classification. Fig. A.2 illustrates the correspodnding water-type maps identified from MSI-derived R_{rs} products (Table 2).

To analyze the spatial and temporal TSS variations at finer scales, SOLID was also applied to three SeaDAS-processed MSI-A images over the San Pablo Bay (Northern San-Francisco-Bay-Delta Estuary, CA) (Fig. 9). The patterns of TSS over the San Pablo Bay are often affected by tides, river discharges, wind, and dredging activities, thereby providing a suitable testbed (Hestir et al., 2013) to evaluate our new retrieval method. Fig. 9a shows an image captured on August 18th 2017 during high tide (GMT 19:03:26). At this time, suspended sediments were all mixed in offshore areas and deposited near the coastline. In contrast, large gradients in sediment concentrations driven by high discharge from the Petaluma River and the Sonoma creek are observed in spring (Fig. 9b March 26th 2018). Finally, another MSI-A image collected on July 24th 2018 2 h before high tide (GMT 19:04:56) showed lower concentrations within the Bay (Fig. 9c), in line with what is expected during flood tide. Prior to high tides, seawater approaches the coast and high sediments are observed to the north. This analysis indicates that the SOLID model provides realistic TSS distribution and is capable of capturing the intra-annual variability in sediment load.

TSS retrievals in eutrophic lakes like Lake Okeechobee and Lake Taihu are further qualitatively assessed. The images were atmospherically corrected using SeaDAS. Due to the presence of high sediment loads, aerosol contributions were compensated for using two SWIR bands (Pahlevan et al., 2017b). The disadvantage of this method is noisy retrievals in areas with lower TSS. Fig. 10 (top row) shows our TSS products derived from MSI-A images over productive waters of Lake Okeechobee. With a mean depth of 3 m together with high-wind events particle resuspension events are quite common (Jin and Ji, 2004). Higher concentrations in the late January map are attributed to prior rain events and commonly high winds in wintertime (Fig. 11). The concentrations are found to be lower in March and April. The spatial distribution of TSS across Lake Taihu is found to be very consistent with previous regional analyses (Zhang, 2014), with higher loads in the central and southern sections of the basin. Evidently, the SOLID model is able to produce spatially congruent TSS maps from MSI images, enabling sound spatio-temporal analyses.

5.4. Extension to other satellite missions

The performance of SOLID for other satellite missions, such as MODIS, VIIRS, OLCI, and OLI is shown in Fig. 11. The corresponding global and water-type specific statistics are provided in Table 6. In general, the statistical metrics are fairly consistent with those reported for MSI (Table 5), indicating potentially interconsistent TSS products derived from various satellite missions made possible through SOLID. The primary difference is attributed to the Bias, which was lower for MSI than the rest of the missions. The largest errors are attributed to OLI-derived TSS products, owing to the absence of spectral information within the 700–800 nm region for approximating spectral b_{bp} (Section 4.1.1). In essence, the overall performance of the MDN model in

estimating b_{bp} at each individual band is better when more relevant spectral features are supplied (Pahlevan et al., 2020), i.e., more accurate b_{bp} is possible via MSI or MODIS than that through OLI (analysis not shown here). A secondary factor that may contribute to the reduced performance of the OLI model is that OLI's red channel, in contrast to other missions, does not fully capture Chl*a* absorption peak at ∼ 670 nm (Table 3). Further, note that R_{rs} spectra that lacked spectral coverage up to 900 nm were excluded for the performance assessment of OLI-like spectra in Type III waters, reducing the number of spectra by nearly one half.

6. Discussion

Following a full assessment of SOLID, it is critical to gauge its sensitivity to the choice of a_{nap}^* in the $b_{bp}(740)$ retrieval scheme (Section 4.1.2) and to the uncertainties in the atmospheric correction. While the former can partly explain algorithm uncertainties in Type III waters, the latter will shed light on uncertainties in TSS products derived from satellite observations. In this section, we will further offer insights into the implementation of SOLID as a standard, global TSS algorithm in coastal and inland waters.

6.1. Non-algal particle absorption (a_{nap})

Using empirical relationships or empiricism in bio-optical modeling or water constituent retrievals is common-practice in ocean color or aquatic remote sensing. For example, best-practice algorithms (Lee et al., 2002; Maritorena et al., 2002; Nechad et al., 2010; Werdell et al., 2013) incorporate various assumptions on the spectral shape and variability of component mass-specific IOPs leading to loss of performance in aquatic environments where empirical relationships may no longer hold (Werdell et al., 2018). Making such assumptions is inevitable due to limited knowledge of the optical properties of myriads of particles in the water column for the design of global algorithms. Although it is recognized that $a_{nap}^*(740)$ varies with type, composition, and size distribution of non-algal particles (Babin and Stramski, 2004; Doxaran et al., 2009b), for simplicity, we chose a constant value for $a_{nap}^*(740) = 0.011$ [m^2/g] (Section 4.1.2). However, by definition $a_{nap}(740)$ ($= a_{nap}^*(740) \times$ TSS) also changes with concentration of particles. To assess the sensitivity of retrieved TSS to variability in $a_{nap}(740)$ in Type III waters, we supplied a broad range of $a_{nap}(740)$, i.e., from zero to 10 [1/m] @ increments of 0.5 [1/m], to the SOLID model. We then analyzed the errors in TSS retrievals expressed as MAE (Eq. (12)) using Type III R_{rs} – TSS pairs ($N = 177$, Table 5). MAE (a unitless, log-based error metric) is a preferred measure because of its straightforward interpretation. From Fig. 12, it can be inferred that MAE reaches a minimum for $1.2 < a_{nap}(740) < 1.6$ [1/m], i.e., the total error in TSS varies from 20 to 60%. Further, MAE tends to increase monotonically for $a_{nap}(740) > 2$ [1/m]. Note that very similar behavior was found when assessing RMSE and MAPE. This assessment suggests that our specific choice of $a_{nap}(740)$ results in small errors in TSS estimations
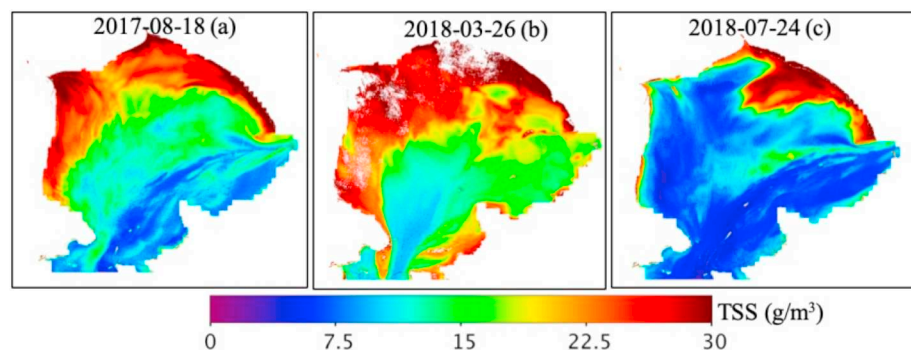

Fig. 9. SeaDAS processed MSI-A images show the spatio-temporal patterns of TSS (derived from SOLID) over the San Pablo Bay (CA). a) Products during summer at high tide on August 18th 2017 (GMT 19:03:26), (b) Image captured during winter season at ebb tide on March 26th 2018 (GMT 19:04:52), and (c) Image obtained during flood tide (2 h before reaching the high tide zone) on July 24th 2018 (GMT 19:04:56).
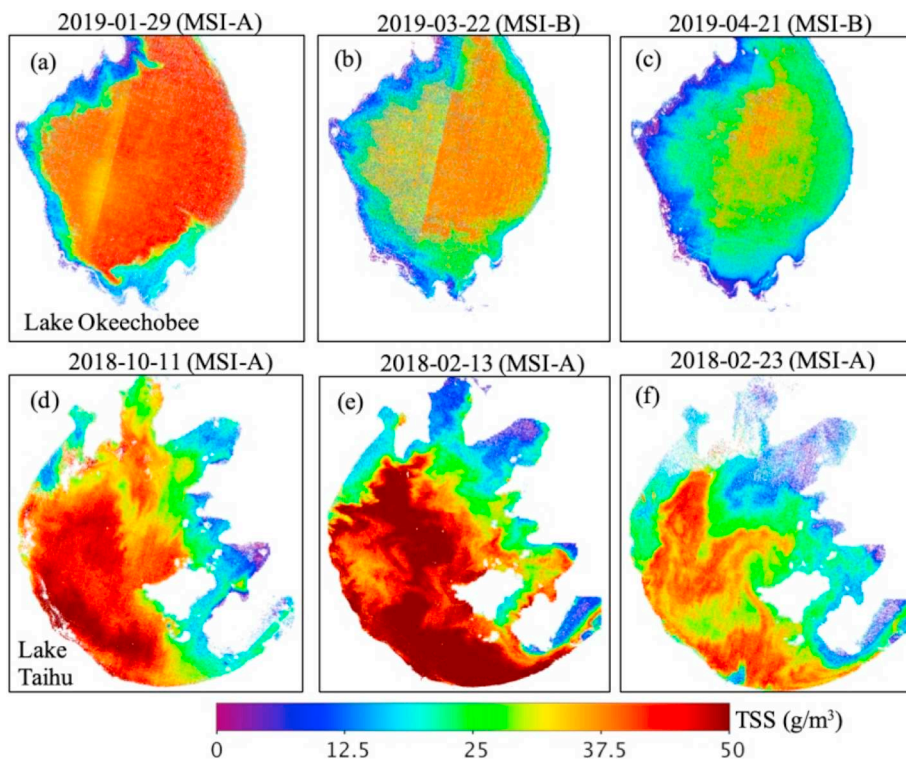
Fig. 10. Spatio-temporal distribution of SOLID retrieved TSS over highly productive lakes such as: (top row) Lake Okeechobee (USA) and (bottom row) Lake Taihu (China) using SeaDAS processed MSIA/B images. (Top row) Transitional variations of TSS are captured during the spring season of 2019 (29th January (a), 22nd March (b) and 21st April (c)). (Bottom row) Spatial dynamics of TSS over Lake Taihu were captured in three different images during 2018 (11th October (d) and 13th February (e), and 23rd February (f)). The images were processed through a SWIR based atmospheric correction procedure (Pahlevan et al., 2017d).

given our validation dataset. A dataset representing extremely higher TSS ($> > 150$ [g/m³]) will likely carry larger uncertainties in TSS retrievals when using SOLID. Hence, care must be taken when interpreting the model outcomes in highly sediment-rich waters.

6.2. Atmospheric correction

Uncertainties in the atmospheric correction are a major source of errors in R_{rs} and the downstream products. These uncertainties emanate from highly turbid/eutrophic conditions, complex aerosols, land/cloud adjacency effects, cloud shadows, and thin clouds (Ngoc et al., 2019; Pahlevan et al., 2017a; Sterckx et al., 2011). Here, the sensitivity of SOLID to uncertainties in the atmospheric correction is analyzed through a Monte Carlo simulation ($n = 1000$). This simulation was carried out by adding Gaussian noise to the most relevant R_{rs} channels and assessing the impacts on downstream TSS products. The MSI's R_{rs} (665) and R_{rs}(740) corresponding to the three water types (Fig. 13; top row) are perturbed by $\delta = 10\%$, which is assumed to be a realistic expected uncertainty in these bands over coastal and inland waters (Pahlevan et al., 2017b). To account for larger uncertainties, we also
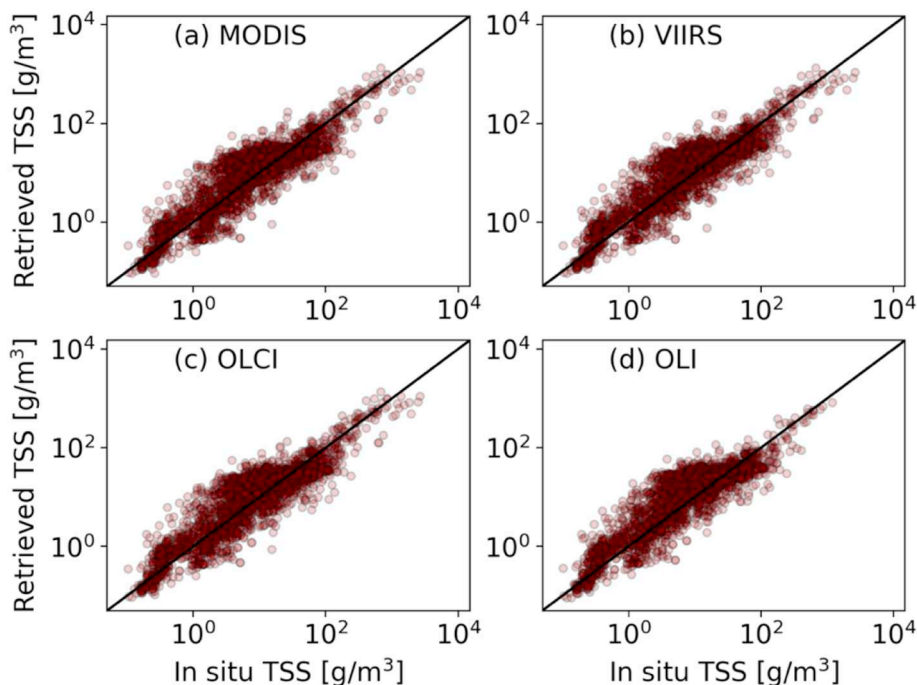

Fig. 11. Scatterplots illustrating the SOLID performance for four different satellite missions. The spectral bands incorporated for retrievals are listed in Table 3.

Table 6
Statistical analysis of TSS retrievals (SOLID) for different satellite missions.

	MAPE [%]	MAE	RMSE	Slope	Bias[a]	N
MODIS	47.33	1.82	0.33	0.96	1.18	2729
VIIRS	49.71	1.84	0.34	0.96	1.24	
OLCI	46.58	1.82	0.33	0.96	1.17	
OLI	52.30	1.87	0.35	0.97	1.34	2633
			Type I			
MODIS	48.69	1.76	0.30	0.95	1.07	430
VIIRS	52.33	1.77	0.31	0.94	1.08	
OLCI	51.23	1.77	0.31	0.93	1.08	
OLI	51.20	1.76	0.31	0.94	1.12	
			Type II			
MODIS	48.46	1.86	0.34	0.88	1.23	2122
VIIRS	51.58	1.90	0.35	0.90	1.30	
OLCI	47.17	1.86	0.35	0.89	1.21	
OLI	54.14	1.91	0.36	0.88	1.42	
			Type III			
MODIS	30.56	1.48	0.22	0.86	0.99	177
VIIRS	31.25	1.47	0.22	0.87	1.00	
OLCI	28.05	1.47	0.22	0.87	0.97	
OLI	25.05	1.39	0.19	0.98	0.85	78

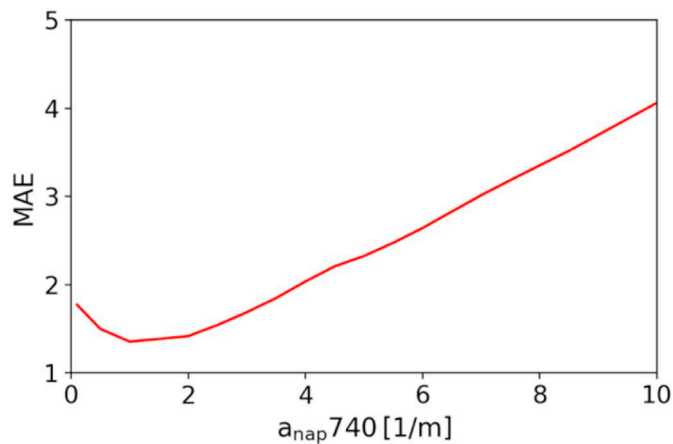[a] Bias = 1 is considered ideal (zero-bias) – see Eq. (11).

Fig. 12. The estimated error (MAE) in TSS retrievals for Type III waters as a function of non-algal particle absorption at 740 nm.

introduce $\delta = 50\%$ to the relevant R_{rs} bands to address the model tolerance to such degrees of uncertainties. The simulated perturbed R_{rs} are then supplied to SOLID for TSS retrievals (Fig. 13; bottom row). Note that, here, we assume that the shape of R_{rs} is valid and the water types are correctly assigned. Fig. 13 illustrates the output histograms with the statistics included in Table 6. Our analysis suggests that the SOLID model produces TSS products with < 21% uncertainties when uncertainties in the corresponding R_{rs} channels are assumed 10%. With $\delta = 50\%$, the uncertainties become too large (Table 7) rendering the derived products unreliable for scientific purposes. Thus, it is critical to ensure high-quality R_{rs} products are retrieved through the atmospheric correction process. Further analyses may be required to assess the performance of SOLID considering biases in the absolute radiometric measurements made by satellite sensors.

6.3. Implications for long-term global monitoring of TSS

Owing to its comparably favorable performance across a wide range of particle loads, the SOLID model has the potential for global retrievals of TSS from a suite of satellite missions that make measurements in the red and NIR spectral regions. Our statistical analysis, however, showed that although the SOLID model outperforms the state-of-the-art models, the overall error, i.e., ~80% gauged via MAE, is yet to be reduced to permit rigorous scientific investigations, where precise estimations of near-surface particle loads are sought. Such magnitudes of error may be ascribed to the complex populations of particles represented by this commonly assessed variable, i.e. ranges of particle sizes and shape and complex optical interactions of the particles. For example, the pigment absorbances of different algal taxa and the formation of flocculant clay-detrital aggregates in the oligohaline reaches of estuaries; these aggregates, in turn, can support a microbial biofilm community of algae and bacteria – imagine the challenges of modeling this phenomenon.

One way to improve SOLID is to use *in situ* data for training MDN to enhance retrievals of b_{bp}. The lack of adequate training data was the main reason for training MDN with simulated data, which may not offer the true representation of bio-optical conditions given limited knowledge of specific IOPs. Alternatively, possible improvements in QAA and GIOP for b_{bp} retrievals in Type I and Type II waters, respectively, may eliminate the necessity for a machine learning model. In addition, uncertainties in the atmospheric correction further preclude precise retrievals of TSS. The performance of SOLID and likely other methods is expected to degrade for large uncertainties in R_{rs} products.

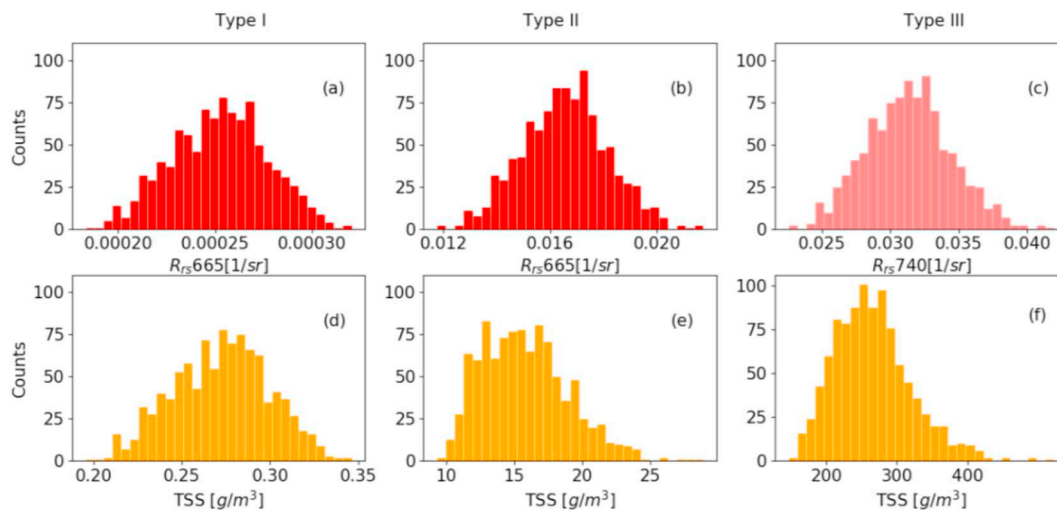To enable production of interconsistent, multimission TSS retrievals

Fig. 13. Gaussian noise distributions ($\delta = 10\%$) used to perturb R_{rs} (top panels) in the red and NIR regions. The output frequency distribution of TSS (lower panels) retrieved from SOLID given the input R_{rs} distributions. (For interpretation of the references to color in this figure legend, the reader is referred to the web version of this article.)

Table 7
Statistics associated with the sensitivity analysis of SOLID to uncertainties in MSI-derived R_{rs} induced by the atmospheric correction. Here, μ and σ are the mean and the standard deviation of the Gaussian distributions. σ_{RD}(%) is the standard deviation of the relative difference.

	δ [%]	R_{rs} [1/sr]		TSS [g/m³]	Output (TSS) distribution		
					μ [g/m³]	σ [g/m³]	σ_{RD} (%)
Type I	10	665 nm	μ = 0.00025 σ = 0.000025	0.275	0.272	0.027	10.1
	50		μ = 0.00025 σ = 0.00013		0.263	0.134	51.0
Type II	10	665 nm	μ = 0.0165 σ = 0.0016	15.04	15.77	3.16	21.1
	50		μ = 0.0165 σ = 0.0082		15.93	19.27	125.1
Type III	10	740 nm	μ = 0.0312 σ = 0.0032	260.49	265.45	54.73	19.5
	50		μ = 0.0312 σ = 0.0156		266.43	1039.9	399.0

at a global scale, one needs to ensure minimal biases exist among TOA observations. Pahlevan et al. (2019) showed that ~ 4% difference in MSI- and OLI-derived R_{rs}(665) translate to ~ 10% difference in TSS products derived via the Nechad model. Prior to generating global TSS products, a comprehensive assessment of image-derived TSS products derived from multiple missions (e.g., MODIS, VIIRS, OLCI, MSI, and OLI) against existing *in situ* databases (e.g., the SeaWiFS Bio-optical Archive and Storage System (SeaBASS), United States Geological Survey's National Water Information System (NWIS)) is required. Given sufficient agreements with *in situ* data, per-retrieval uncertainty should be computed and produced alongside TSS values. This can be achieved through Monte Carlo simulations and the training of a model to provide uncertainty estimates in a computationally inexpensive fashion.

7. Conclusion

The primary goal of this study has been to introduce a hybrid scheme for TSS retrievals that would advance the state-of-the-art for TSS retrievals in both inland and coastal waters. This strategy referred to as SOLID applies water-type-specific algorithms to provide an estimation of TSS for a given $R_{rs}(\lambda)$ by retrieving b_{bp} in the red/NIR region as intermediate products. The water types determined given R_{rs}(400 nm < λ < 700 nm) constitute blue-green waters (Type I), green waters (Type II), and sediment-laden brown waters (Type III). For b_{bp} inversion in Type II waters, we apply a machine learning model that enhances b_{bp} estimates compared to widely used semi-analytical methods (e.g., QAA and GIOP). Through an extensive validation exercise, we show that SOLID outperforms the state-of-the-art algorithms across a wide range of TSS, i.e., 0.10–2626.8 [g/m³], suggesting its potential utility for global mapping of TSS. The global statistics, including MAPE (49%), RMSE (0.32), MAE (1.81), and Bias (1.09), corroborate that the SOLID model improves retrieval performances offered by several widely used TSS retrieval methods. In particular, the performance of SOLID is superior to that of Nechad et al. (2010) and Novoa et al. (2017) in both Type I and Type III waters by a noticeable margin. We show that the model is anticipated to perform well for various missions, such as MSI, OLCI, MODIS, VIIRS, and OLI. The primary confounding factor for mass production of TSS products is believed to be the uncertainties in the atmospheric correction, i.e., we demonstrate that 10% uncertainties in R_{rs}(600 nm < λ < 800 nm) result in ~ 20% uncertainties in TSS. Considering its fairly consistent performance across multiple missions, this model can be utilized operationally for generating products subject to an extensive satellite matchup assessment in coastal and inland waters. Although the SOLID model is found

in our analysis to perform better than the existing algorithms, there still remains an ~ 80% error in global TSS retrievals. Contingent upon the availability of high-fidelity *in situ* data, machine-learning approaches shall be explored to further reduce such uncertainties.

CRediT authorship contribution statement

Sundarabalan V. Balasubramanian: Formal analysis, Investigation, Methodology, Software, Validation, Visualization. **Nima Pahlevan:** Conceptualization, Funding acquisition, Project administration, Resources, Supervision, Writing - original draft, Writing - review & editing. **Brandon Smith:** Methodology, Software. **Caren Binding:** Data curation, Writing - review & editing. **John Schalles:** Data curation. **Hubert Loisel:** Data curation. **Daniela Gurlin:** Data curation. **Steven Greb:** Data curation. **Krista Alikas:** Data curation. **Mirjam Randla:** Data curation. **Matsushita Bunkei:** Data curation. **Wesley Moses:** Data curation. **Hà Nguyễn:** Data curation. **Moritz K. Lehmann:** Data curation. **David O'Donnell:** Data curation. **Michael Ondrusek:** Data curation. **Tai-Hyun Han:** Data curation. **Cédric G. Fichot:** Data curation. **Tim Moore:** Data curation. **Emmanuel Boss**: Writing - review & editing.

Declaration of competing interest

The authors declare that they have no known competing financial interests or personal relationships that could have appeared to influence the work reported in this paper.
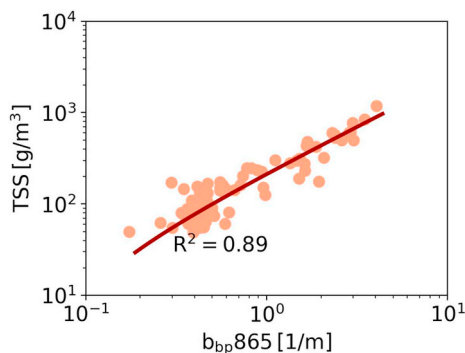
Appendix A

Fig. A.1. Scatterplot corresponding to *in situ* TSS and $b_{bp}(865)$ datasets developed for OLI observations in Type III waters. Note that the fitted lines are displayed in log-log scale.
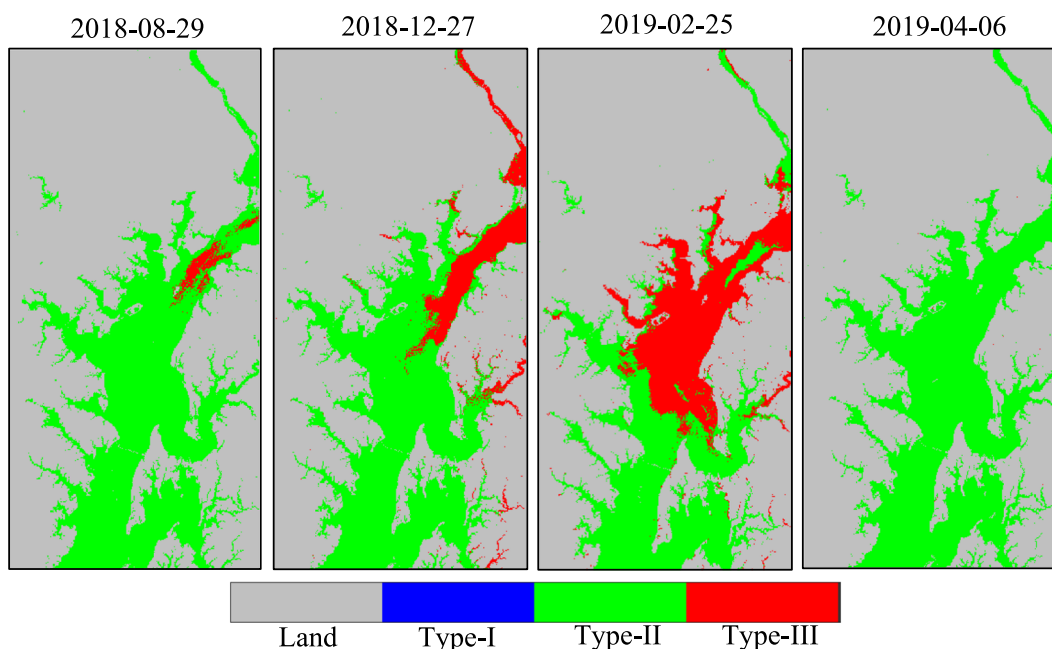

Fig. A.2. Chesapeake Bay water-type maps corresponding to MSI images shown in Fig. 8. As expected, the upper bay area is commonly assigned to Type III and the mid and lower bay regions are classified as Type II waters. Type I waters are not found in the bay for these four dates.

The performance of MDN against that of GIOP and QAA is further elaborated. Evidently, MDN-based b_{bp} retrievals are consistently better than those determined by both GIOP and QAA; hence, MDN may be regarded as an alternative to these heritage algorithms in turbid and/or eutrophic ecosystems in coastal and inland waters with $b_{bp}(665)$ ranging from 0.05 to 0.5 [1/m] (see Section 5.1).

Table A1
The performance of GIOP, QAA, and MDN for b_{bp} retrievals across all MSI visible bands for Type II waters. Best statistical descriptors in each category are boldfaced.

	MAPE [%]	MAE	RMSE	Slope	Bias[a]
			443 nm		
GIOP	42.55	1.81	0.33	0.76	0.67
QAA	50.72	1.74	0.30	**0.80**	1.36
MDN	**36.51**	**1.57**	**0.26**	0.76	**1.08**
			490 nm		
GIOP	41.18	1.74	0.30	0.78	0.70
QAA	50.01	1.71	0.29	**0.83**	1.40
MDN	**36.34**	**1.53**	**0.24**	0.80	**1.10**
			560 nm		
GIOP	36.01	1.61	0.26	0.82	0.74
QAA	58.74	1.72	0.28	**0.86**	1.50
MDN	**37.37**	**1.53**	**0.23**	0.81	**1.20**
			665 nm		
GIOP	**28.94**	1.52	0.24	0.85	0.78

(continued on next page)

Table A1 (*continued*)

	MAPE [%]	MAE	RMSE	Slope	Bias[a]
QAA	62.70	1.76	0.29	**0.90**	1.58
MDN	33.15	**1.47**	**0.21**	0.84	**1.11**

[a] Bias = 1 is considered ideal (zero-bias) – see Eq. (11).

Table A2

Expressions used in this study for the assessment of state-of-the-art TSS models.

Model	Relation	Source
Miller-McKee	$(1140.25\ R_{rs}(668))\ {-}1.91$	(Miller and McKee, 2004)
Nechad	$1.74 + (355.85\rho_w(665))/(1{-}(\rho_w(665)/1728))$	(Nechad et al., 2010)
Petus	$\{12450 R_{rs}(668)^2\} + 666.1\{R_{rs}(668)\} + 0.4$	(Petus et al., 2010)
Ondrusek	$3.8813 nL_w(665)^3 {-}13.822 nL_w(665)^2 + 19.61 nL_w(665)$	(Ondrusek et al., 2012)
Novoa	$531.5 \times \rho_w(665)$ (Type-I&II)	(Novoa et al., 2017)
	$\{37{,}150 \times \rho_w(865)^2\} +.\ \{1751 \times \rho_w(865)\}$ (Type-III)	

References

Agarap, A.F., 2018. Deep Learning using Rectified Linear Units (ReLU). *arXiv preprint arXiv:1803.08375*.

Ahn, Y.H., Shanmugam, P., Moon, J.E., 2006. Retrieval of ocean colour from high resolution multi-spectral imagery for monitoring highly dynamic ocean features. Int. J. Remote Sens. 27, 367–392.

Aurin, D.A., Dierssen, H.M., 2012. Advantages and limitations of ocean color remote sensing in CDOM-dominated, mineral-rich coastal and estuarine waters. Remote Sens. Environ. 125, 181–197.

Babin, M., Stramski, D., 2004. Variations in the mass-specific absorption coefficient of mineral particles suspended in water. Limnol. Oceanogr. 49, 756–767.

Babin, M., Stramski, D., Ferrari, G.M., Claustre, H., Bricaud, A., Obolensky, G., Hoepffner, N., 2003. Variations in the light absorption coefficients of phytoplankton, nonalgal particles, and dissolved organic matter in coastal waters around Europe. J. Geophys. Res. Oceans 108.

Barbier, E.B., Hacker, S.D., Kennedy, C., Koch, E.W., Stier, A.C., Silliman, B.R., 2011. The value of estuarine and coastal ecosystem services. Ecol. Monogr. 81, 169–193.

Binding, C., Jerome, J., Bukata, R., Booty, W., 2010. Suspended particulate matter in Lake Erie derived from MODIS aquatic colour imagery. Int. J. Remote Sens. 31, 5239–5255.

Binding, C., Zastepa, A., Zeng, C., 2019. The impact of phytoplankton community composition on optical properties and satellite observations of the 2017 western Lake Erie algal bloom. J. Great Lakes Res. 45, 573–586.

Bishop, C.M., 1994. Mixture Density Networks. NCRG/94/004. Aston University Birmingham. http://www.ncrg.aston.ac.uk.

Bowers, D., Binding, C., 2006. The optical properties of mineral suspended particles: a review and synthesis. Estuar. Coast. Shelf Sci. 67, 219–230.

Bukata, R.P., Jerome, J.H., Kondratyev, A.S., Pozdnyakov, D.V., 2018. Optical Properties and Remote Sensing of Inland and Coastal Waters. CRC press.

Casey, Kimberly, et al., 2019. A global compilation of in situ aquatic high spectral resolution inherent and apparent optical property data for remote sensing applications. Earth Syst. Sci. Data Discuss. 1–29. https://doi.org/10.5194/essd-2019-105.

Chen, S., Han, L., Chen, X., Li, D., Sun, L., Li, Y., 2015. Estimating wide range total suspended solids concentrations from MODIS 250-m imageries: an improved method. ISPRS J. Photogramm. Remote Sens. 99, 58–69.

D'Alimonte, D., Zibordi, G., Berthon, J.-F., Canuti, E., Kajiyama, T., 2012. Performance and applicability of bio-optical algorithms in different European seas. Remote Sens. Environ. 124, 402–412.

Dekker, A.G., Vos, R.J., Peters, S.W.M., 2001. Comparison of remote sensing data, model results and in situ data for total suspended matter (TSM) in the southern Frisian lakes. Sci. Total Environ. 268, 197–214.

Dekker, A.G., Vos, R., Peters, S., 2002. Analytical algorithms for lake water TSM estimation for retrospective analyses of TM and SPOT sensor data. Int. J. Remote Sens. 23, 15–35.

Dogliotti, A.I., Ruddick, K., Nechad, B., Doxaran, D., Knaeps, E., 2015. A single algorithm to retrieve turbidity from remotely-sensed data in all coastal and estuarine waters. Remote Sens. Environ. 156, 157–168.

Doxaran, D., Froidefond, J.-M., Castaing, P., 2003. Remote-sensing reflectance of turbid sediment-dominated waters. Reduction of sediment type variations and changing illumination conditions effects by use of reflectance ratios. Appl. Opt. 42, 2623–2634.

Doxaran, D., Froidefond, J.-M., Castaing, P., Babin, M., 2009a. Dynamics of the turbidity maximum zone in a macrotidal estuary (the Gironde, France): observations from field and MODIS satellite data. Estuar. Coast. Shelf Sci. 81, 321–332.

Doxaran, D., Ruddick, K., McKee, D., Gentili, B., Tailliez, D., Chami, M., Babin, M., 2009b. Spectral variations of light scattering by marine particles in coastal waters, from the visible to the near infrared. Limnol. Oceanogr. 54, 1257–1271.

Doxaran, D., Ehn, J., Bélanger, S., Matsuoka, A., Hooker, S., Babin, M., 2012. Optical characterisation of suspended particles in the Mackenzie River plume (Canadian Arctic Ocean) and implications for ocean colour remote sensing. Biogeosciences 9, 3213–3229.

Doxaran, D., Lamquin, N., Park, Y.-J., Mazeran, C., Ryu, J.-H., Wang, M., Poteau, A., 2014. Retrieval of the seawater reflectance for suspended solids monitoring in the East China Sea using MODIS, MERIS and GOCI satellite data. Remote Sens. Environ. 146, 36–48.

Doxaran, D., Leymarie, E., Nechad, B., Dogliotti, A., Ruddick, K., Gernez, P., Knaeps, E., 2016. Improved correction methods for field measurements of particulate light backscattering in turbid waters. Opt. Express 24, 3615–3637.

Estapa, M.L., Boss, E., Mayer, L.M., Roesler, C.S., 2012. Role of iron and organic carbon in mass-specific light absorption by particulate matter from Louisiana coastal waters. Limnol. Oceanogr. 57, 97–112.

Feng, L., Hu, C., Chen, X., Song, Q., 2014. Influence of the Three Gorges Dam on total suspended matters in the Yangtze estuary and its adjacent coastal waters: observations from MODIS. Remote Sens. Environ. 140, 779–788.

Forget, P., Ouillon, S., 1998. Surface suspended matter off the Rhone river mouth from visible satellite imagery. Oceanol. Acta 21, 739–749.

Fugate, D.C., Friedrichs, C.T., Sanford, L.P., 2007. Lateral dynamics and associated transport of sediment in the upper reaches of a partially mixed estuary, Chesapeake Bay, USA. Cont. Shelf Res. 27, 679–698.

Gernez, P., Barillé, L., Lerouxel, A., Mazeran, C., Lucas, A., Doxaran, D., 2014. Remote sensing of suspended particulate matter in turbid oyster-farming ecosystems. J. Geophys. Res. Oceans 119, 7277–7294.

Gitelson, A.A., Dall'Olmo, G., Moses, W., Rundquist, D.C., Barrow, T., Fisher, T.R., Gurlin, D., Holz, J., 2008. A simple semi-analytical model for remote estimation of chlorophyll-a in turbid waters: validation. Remote Sens. Environ. 112, 3582–3593.

Gordon, H.R., Wang, M., 1994. Retrieval of water-leaving radiance and aerosol optical thickness over the oceans with SeaWiFS: a preliminary algorithm. Appl. Opt. 33, 443–452.

Gordon, H.R., Brown, O.B., Evans, R.H., Brown, J.W., Smith, R.C., Baker, K.S., Clark, D.K., 1988. A semianalytic radiance model of ocean color. J. Geophys. Res.-Atmos. 93, 10909–10924.

Han, B., Loisel, H., Vantrepotte, V., Mériaux, X., Bryère, P., Ouillon, S., Dessailly, D., Xing, Q., Zhu, J., 2016. Development of a semi-analytical algorithm for the retrieval of suspended particulate matter from remote sensing over clear to very turbid waters. Remote Sens. 8, 211.

Hannouche, A., Joannis, C., Chebbo, G., 2017. Assessment of total suspended solids (TSS) event load and its uncertainties in combined sewer system from continuous turbidity measurements. Urban Water J. 14, 789–796.

Hestir, E.L., Schoellhamer, D.H., Morgan-King, T., Ustin, S.L., 2013. A step decrease in sediment concentration in a highly modified tidal river delta following the 1983 El Niño floods. Mar. Geol. 345, 304–313.

Ioannou, I., Gilerson, A., Gross, B., Moshary, F., Ahmed, S., 2011. Neural network approach to retrieve the inherent optical properties of the ocean from observations of MODIS. Appl. Opt. 50, 3168–3186.

Jin, K.-R., Ji, Z.-G., 2004. Case study: modeling of sediment transport and wind-wave impact in Lake Okeechobee. J. Hydraul. Eng. 130, 1055–1067.

Joshi, I.D., D'Sa, E.J., 2018. An estuarine-tuned quasi-analytical algorithm (QAA-V): assessment and application to satellite estimates of SPM in Galveston Bay following hurricane Harvey. Biogeosciences 15, 4065–4086.

Kemp, W.M., Boynton, W.R., Adolf, J.E., Boesch, D.F., Boicourt, W.C., Brush, G., Cornwell, J.C., Fisher, T.R., Glibert, P.M., Hagy, J.D., 2005. Eutrophication of Chesapeake Bay: historical trends and ecological interactions. Mar. Ecol. Prog. Ser. 303, 1–29.

Knaeps, E., Ruddick, K., Doxaran, D., Dogliotti, A.I., Nechad, B., Raymaekers, D., Sterckx, S., 2015. A SWIR based algorithm to retrieve total suspended matter in extremely turbid waters. Remote Sens. Environ. 168, 66–79.

Knaeps, E., Doxaran, D., Dogliotti, A., Nechad, B., Ruddick, K., Raymaekers, D., Sterckx,

S., 2018. The SeaSWIR dataset. Earth System Science Data 10, 1439–1449.

Kumar, A., Equeenuddin, S.M., Mishra, D.R., Acharya, B.C., 2016. Remote monitoring of sediment dynamics in a coastal lagoon: Long-term spatio-temporal variability of suspended sediment in Chilika. Estuar. Coast. Shelf Sci. 170, 155–172.

Lee, Z., Carder, K.L., Arnone, R.A., 2002. Deriving inherent optical properties from water color: a multiband quasi-analytical algorithm for optically deep waters. Appl. Opt. 41, 5755–5772.

Lee, Z., Pahlevan, N., Ahn, Y.-H., Greb, S., O'Donnell, D., 2013. Robust approach to directly measuring water-leaving radiance in the field. Appl. Opt. 52, 1693–1701.

Loisel, H., Morel, A., 2001. Non-isotropy of the upward radiance field in typical coastal (case 2) waters. Int. J. Remote Sens. 22, 275–295.

Loisel, H., Mangin, A., Vantrepotte, V., Dessailly, D., Dinh, D.N., Garnesson, P., Ouillon, S., Lefebvre, J.-P., Mériaux, X., Phan, T.M., 2014. Variability of suspended particulate matter concentration in coastal waters under the Mekong's influence from ocean color (MERIS) remote sensing over the last decade. Remote Sens. Environ. 150, 218–230.

Long, C.M., Pavelsky, T.M., 2013. Remote sensing of suspended sediment concentration and hydrologic connectivity in a complex wetland environment. Remote Sens. Environ. 129, 197–209.

Luo, Y., Doxaran, D., Ruddick, K., Shen, F., Gentili, B., Yan, L., Huang, H., 2018. Saturation of water reflectance in extremely turbid media based on field measurements, satellite data and bio-optical modelling. Opt. Express 26, 10435–10451.

Maritorena, S., Siegel, D.A., Peterson, A.R., 2002. Optimization of a semianalytical ocean color model for global-scale applications. Appl. Opt. 41, 2705–2714.

Miller, R.L., McKee, B.A., 2004. Using MODIS Terra 250 m imagery to map concentrations of total suspended matter in coastal waters. Remote Sens. Environ. 93, 259–266.

Mitchell, C., Cunningham, A., McKee, D., 2016. Derivation of the specific optical properties of suspended mineral particles and their contribution to the attenuation of solar irradiance in offshore waters by ocean color remote sensing. J. Geophys. Res. Oceans 121, 104–117.

Mobley, C.D., 1999. Estimation of the remote-sensing reflectance from above-surface measurements. Appl. Opt. 38, 7442–7455.

Mobley, C.D., Sundman, L.K., 2008. Hydrolight 5, Ecolight5 User Guide. Sequoia Scientific, Inc.

Moore, T.S., Mouw, C.B., Sullivan, J.M., Twardowski, M.S., Burtner, A.M., Ciochetto, A.B., McFarland, M.N., Nayak, A.R., Paladino, D., Stockley, N.D., Johengen, T.H., Yu, A.W., Ruberg, S., Weidemann, A., 2017. Bio-optical properties of cyanobacteria blooms in Western Lake Erie. Front. Mar. Sci. 4.

Morel, A., Prieur, L., 1977. Analysis of variations in ocean color 1. Limnol. Oceanogr. 22, 709–722.

Morel, A., Voss, K.J., Gentili, B., 1995. Bidirectional reflectance of oceanic waters: a comparison of modeled and measured upward radiance fields. J. Geophys. Res. Oceans 100, 13143–13150.

Mouw, C.B., Chen, H., McKinley, G.A., Effler, S., O'Donnell, D., Perkins, M.G., Strait, C., 2013. Evaluation and optimization of bio-optical inversion algorithms for remote sensing of Lake Superior's optical properties. J. Geophys. Res. Oceans 118, 1696–1714.

Mueller, J.L., Fargion, G.S., McClain, C.R., Mueller, J., Brown, S., Clark, D., Johnson, B., Yoon, H., Lykke, K., Flora, S., 2004. Ocean optics protocols for satellite ocean color sensor validation, revision 5, volume VI: special topics in ocean optics protocols, part 2. NASA Report 211621 (2003), 1–36.

Nechad, B., Ruddick, K., Park, Y., 2010. Calibration and validation of a generic multi-sensor algorithm for mapping of total suspended matter in turbid waters. Remote Sens. Environ. 114, 854–866.

Neukermans, G., Ruddick, K.G., Greenwood, N., 2012. Diurnal variability of turbidity and light attenuation in the southern North Sea from the SEVIRI geostationary sensor. Remote Sens. Environ. 124, 564–580.

Ngoc, D.D., Loisel, H., Jamet, C., Vantrepotte, V., Duforêt-Gaurier, L., Minh, C.D., Mangin, A., 2019. Coastal and inland water pixels extraction algorithm (WiPE) from spectral shape analysis and HSV transformation applied to Landsat 8 OLI and Sentinel-2 MSI. Remote Sens. Environ. 223, 208–228.

Novo, E., Hansom, J., Curran, P., 1989. The effect of sediment type on the relationship between reflectance and suspended sediment concentration. Remote Sens. 10, 1283–1289.

Novoa, S., Doxaran, D., Ody, A., Vanhellemont, Q., Lafon, V., Lubac, B., Gernez, P., 2017. Atmospheric corrections and multi-conditional algorithm for multi-sensor remote sensing of suspended particulate matter in low-to-high turbidity levels coastal waters. Remote Sens. 9, 61.

Ondrusek, M., Stengel, E., Kinkade, C.S., Vogel, R.L., Keegstra, P., Hunter, C., Kim, C., 2012. The development of a new optical total suspended matter algorithm for the Chesapeake Bay. Remote Sens. Environ. 119, 243–254.

Ouillon, S., Douillet, P., Andréfouët, S., 2004. Coupling satellite data with in situ measurements and numerical modeling to study fine suspended-sediment transport: a study for the lagoon of New Caledonia. Coral Reefs 23, 109–122.

Oyama, Y., Matsushita, B., Fukushima, T., Matsushige, K., Imai, A., 2009. Application of spectral decomposition algorithm for mapping water quality in a turbid lake (Lake Kasumigaura, Japan) from Landsat TM data. ISPRS J. Photogramm. Remote Sens. 64, 73–85.

Pahlevan, N., Roger, J.-C., Ahmad, Z., 2017a. Revisiting short-wave-infrared (SWIR) bands for atmospheric correction in coastal waters. Opt. Express 25, 6015–6035.

Pahlevan, N., Sarkar, S., Franz, B.A., Balasubramanian, S.V., He, J., 2017b. Sentinel-2 MultiSpectral instrument (MSI) data processing for aquatic science applications: demonstrations and validations. Remote Sens. Environ. 201, 47–56.

Pahlevan, N., Schott, J.R., Franz, B.A., Zibordi, G., Markham, B., Bailey, S., Schaaf, C.B., Ondrusek, M., Greb, S., Strait, C.M., 2017c. Landsat 8 remote sensing reflectance (R rs) products: evaluations, intercomparisons, and enhancements. Remote Sens.

Environ. 190, 289–301.

Pahlevan, N., Smith, B., Binding, C., O'Donnell, D.M., 2017d. Spectral band adjustments for remote sensing reflectance spectra in coastal/inland waters. Opt. Express 25, 28650–28667.

Pahlevan, N., Chittimalli, S.K., Balasubramanian, S.V., Vellucci, V., 2019. Sentinel-2/ Landsat-8 product consistency and implications for monitoring aquatic systems. Remote Sens. Environ. 220, 19–29.

Pahlevan, N., Smith, B., Schalles, J., Binding, C., Cao, Z., Ma, R., Alikas, K., Kangro, K., Gurlin, D., Hà, N., Matsushita, B., Moses, W., Greb, S., Lehmann, M., Ondrusek, M., Oppelt, N., Stumpf, R., 2020. Seamless retrievals of chlorophyll-a from Sentinel-2 (MSI) and Sentinel-3 (OLCI) in inland and coastal waters: a machine-learning approach. Remote Sens. Environ. 111604.

Petus, C., Chust, G., Gohin, F., Doxaran, D., Froidefond, J.-M., Sagarminaga, Y., 2010. Estimating turbidity and total suspended matter in the Adour River plume (South Bay of Biscay) using MODIS 250-m imagery. Cont. Shelf Res. 30, 379–392.

Pham, Q., Ha, N., Pahlevan, N., Oanh, L., Nguyen, T., Nguyen, N., 2018. Using Landsat-8 images for quantifying suspended sediment concentration in Red River (northern Vietnam). Remote Sens. 10, 1841.

Pope, R.M., Fry, E.S., 1997. Absorption spectrum (380–700 nm) of pure water. II. Integrating cavity measurements. Appl. Opt. 36, 8710–8723.

Reynolds, R.A., Stramski, D., Neukermans, G., 2016. Optical backscattering by particles in Arctic seawater and relationships to particle mass concentration, size distribution, and bulk composition. Limnol. Oceanogr. 61, 1869–1890.

Ritchie, J.C., Zimba, P.V., Everitt, J.H., 2003. Remote sensing techniques to assess water quality. Photogramm. Eng. Remote. Sens. 69, 695–704.

Schalles, J.F., 2006. Optical remote sensing techniques to estimate phytoplankton chlorophyll a concentrations in coastal. Remote Sensing of Aquatic Coastal Ecosystem Processes 27–79 (Springer).

Shanmugam, P., Ahn, Y.-H., Ryu, J.-H., Sundarabalan, B., 2010. An evaluation of inversion models for retrieval of inherent optical properties from ocean color in coastal and open sea waters around Korea. J. Oceanogr. 66, 815–830.

Shi, W., Wang, M., 2009. An assessment of the black ocean pixel assumption for MODIS SWIR bands. Remote Sens. Environ. 113, 1587–1597.

Shi, W., Zhang, Y., Wang, M., 2018. Deriving total suspended matter concentration from the near-infrared-based inherent optical properties over turbid waters: a case study in Lake Taihu. Remote Sens. 10, 333.

Siswanto, E., Tang, J., Yamaguchi, H., Ahn, Y.-H., Ishizaka, J., Yoo, S., Kim, S.-W., Kiyomoto, Y., Yamada, K., Chiang, C., 2011. Empirical ocean-color algorithms to retrieve chlorophyll-a, total suspended matter, and colored dissolved organic matter absorption coefficient in the Yellow and East China Seas. J. Oceanogr. 67, 627–650.

Smith, R.C., Baker, K.S., 1978. Optical classification of natural waters 1. Limnol. Oceanogr. 23, 260–267.

Sterckx, S., Knaeps, E., Ruddick, K., 2011. Detection and correction of adjacency effects in hyperspectral airborne data of coastal and inland waters: the use of the near infrared similarity spectrum. Int. J. Remote Sens. 32, 6479–6505.

Sydor, M., Gould, R.W., Arnone, R.A., Haltrin, V.I., Goode, W., 2004. Uniqueness in remote sensing of the inherent optical properties of ocean water. Appl. Opt. 43, 2156–2162.

Tassan, S., 1993. An improved in-water algorithm for the determination of chlorophyll and suspended sediment concentration from thematic mapper data in coastal waters. Int. J. Remote Sens. 14, 1221–1229.

Turner, A., Millward, G., 2002. Suspended particles: their role in estuarine biogeochemical cycles. Estuar. Coast. Shelf Sci. 55, 857–883.

Vanhellemont, Q., Ruddick, K., 2014. Turbid wakes associated with offshore wind turbines observed with Landsat 8. Remote Sens. Environ. 145, 105–115.

Volpe, V., Silvestri, S., Marani, M., 2011. Remote sensing retrieval of suspended sediment concentration in shallow waters. Remote Sens. Environ. 115, 44–54.

Wang, W.-q., Dong, Q., Shang, S.-l., Wu, J.-y., Lee, Z.-p., 2009. An evaluation of two semi-analytical ocean color algorithms for waters of the South China Sea. J. Trop. Oceanogr. 28, 36–42.

Wei, J., Lee, Z., Shang, S., 2016. A system to measure the data quality of spectral remote-sensing reflectance of aquatic environments. J. Geophys. Res. Oceans 121, 8189–8207.

Werdell, P.J., Bailey, S.W., 2005. An improved in-situ bio-optical data set for ocean color algorithm development and satellite data product validation. Remote Sens. Environ. 98, 122–140.

Werdell, P.J., Franz, B.A., Bailey, S.W., 2010. Evaluation of shortwave infrared atmospheric correction for ocean color remote sensing of Chesapeake Bay. Remote Sens. Environ. 114, 2238–2247.

Werdell, P.J., Franz, B.A., Bailey, S.W., Feldman, G.C., Boss, E., Brando, V.E., Dowell, M., Hirata, T., Lavender, S.J., Lee, Z., 2013. Generalized ocean color inversion model for retrieving marine inherent optical properties. Appl. Opt. 52, 2019–2037.

Werdell, P.J., McKinna, L.I., Boss, E., Ackleson, S.G., Craig, S.E., Gregg, W.W., Lee, Z., Maritorena, S., Roesler, C.S., Rousseaux, C.S., 2018. An overview of approaches and challenges for retrieving marine inherent optical properties from ocean color remote sensing. Prog. Oceanogr. 160, 186–212.

Weston, N.B., 2014. Declining sediments and rising seas: an unfortunate convergence for tidal wetlands. Estuar. Coasts 37, 1–23.

Woźniak, S.B., Stramski, D., 2004. Modeling the optical properties of mineral particles suspended in seawater and their influence on ocean reflectance and chlorophyll estimation from remote sensing algorithms. Appl. Opt. 43, 3489–3503.

Woźniak, S.B., Stramski, D., Stramska, M., Reynolds, R.A., Wright, V.M., Miksic, E.Y., Cichocka, M., Cieplak, A.M., 2010. Optical variability of seawater in relation to particle concentration, composition, and size distribution in the nearshore marine environment at Imperial Beach, California. J. Geophys. Res. Oceans 115.

Yang, W., Matsushita, B., Chen, J., Fukushima, T., 2011. Estimating constituent

concentrations in case II waters from MERIS satellite data by semi-analytical model optimizing and look-up tables. Remote Sens. Environ. 115, 1247–1259.

Zhang, Y., et al., 2014. Lake topography and wind waves determining seasonal-spatial dynamics of total suspended matter in turbid Lake Taihu, China: assessment using long-term high-resolution MERIS. PloS one 9 (5). https://doi.org/10.1371/journal.pone.0098055.

Zhang, M., Tang, J., Dong, Q., Song, Q., Ding, J., 2010. Retrieval of total suspended matter concentration in the yellow and East China seas from MODIS imagery. Remote Sens. Environ. 114, 392–403.

Zhang, Y., Zhang, Y., Shi, K., Zha, Y., Zhou, Y., Liu, M., 2016. A Landsat 8 OLI-based, semianalytical model for estimating the total suspended matter concentration in the slightly turbid Xin'anjiang reservoir (China). IEEE journal of selected topics in applied earth observations and remote sensing 9, 398–413.

Zheng, G., DiGiacomo, P.M., 2017. Uncertainties and applications of satellite-derived coastal water quality products. Prog. Oceanogr. 159, 45–72.

Zheng, G., Stramski, D., Reynolds, R.A., 2014. Evaluation of the quasi-analytical algorithm for estimating the inherent optical properties of seawater from ocean color: comparison of Arctic and lower-latitude waters. Remote Sens. Environ. 155, 194–209.